Salisbury, M. H., Scott, J. H., et al., 1988
Proceedings of the Ocean Drilling Program, Scientific Results, Vol. 102

8. STRUCTURE OF UPPER OCEANIC CRUST FROM AN OBLIQUE SEISMIC EXPERIMENT AT HOLE 418A, WESTERN NORTH ATLANTIC[1]

Stephen A. Swift, Ralph A. Stephen, and Hartley Hoskins, Woods Hole Oceanographic Institution, Woods Hole, Massachusetts[2]

ABSTRACT

During the return to Hole 418A (110 Ma, magnetic anomaly *M0*) of ODP Leg 102, a three-component seismometer was clamped at five depths within oceanic basement. At most seismometer depths shots were aligned on eight radial lines and four concentric circles, ranging up to 8 km. Over 2200 *P*-wave arrival times were picked. Traveltimes from the radial lines were inverted to give a velocity-depth profile by τ-ζ inversion and an inflection point method. Compressional velocity increases nearly linearly at a gradient of $\pm 1.5\ s^{-1}$ from 4.5 km/s at top of basement to 6.8 km/s at a depth of 1.5 km. Below ~0.2 km our velocities are 0.25–0.5 km/s less than sonic-log velocities, suggesting local lithology or crack porosity drilled at Hole 418A may not be representative of the upper crust within ~5 km. At 0.5–1.3 km depth our velocities are ~0.25 km/s less than τ-ζ inversion velocities at nearby Hole 417D. Traveltimes from shots on circular lines indicate that *P*-wave anisotropy (180° period) of ±0.22 km/s (~5%) in the upper 0.5 km is restricted to within ~0.6 km of the hole. The horizontal symmetry axis is oblique to the paleospreading direction and rotates counterclockwise with increasing seismometer depth. Significant anisotropy with a 180° period does not extend beyond a ~0.6-km range within the upper 0.5 km of crust and does not occur at depths of 0.5–1.5 km over ranges of 4–6 km.

INTRODUCTION

An oblique seismic experiment (OSE) differs from conventional marine seismic-refraction studies in that the receiver is placed within upper oceanic crust, the layer being studied, rather than at the seafloor or at the sea surface. In practice, this receiver is a three-component seismometer sequentially coupled at several depths within a basement borehole. The primary advantages are (1) no direct water-wave arrival to obscure arrivals from shallow crust at short range, (2) better signal-to-noise ratio than seafloor receivers owing to direct coupling to basement rocks, (3) unique shallow crustal velocity measurements from observation of the decay of the "direct root" phase (Stephen and Bolmer, 1985) and from an analysis of the inflection point in the traveltime-range plot (Stephen and Harding, 1983), and (4) reduced uncertainty in receiver location. With several borehole receiver depths and closely spaced air gun shots (e.g., 0.1–0.2 km), an OSE can yield seismic velocity models to depths of ~2 km over ranges of 0.5–10 km; resolution is limited only by the seismic wavelength (0.1–0.5 km) and the bandwidth of the source (5–50 Hz). This scale of resolution is intermediate between that of conventional marine seismic surveys and borehole logging studies. The primary objective, then, of an OSE is to obtain a seismic structure model of upper oceanic crust on a scale of hundreds of meters to a few kilometers, which can be compared directly to samples and logs from a borehole.

Current models of the seismic structure of upper oceanic crust (Layer 2) are in general agreement that *P*-wave velocity increases from 2.5–5 km/s at the top of igneous crust to ~6 km/s at depths of 2–3 km (gradients up to 3 s^{-1}; Spudich and Orcutt, 1980a; Purdy and Ewing, 1986). Ophiolite studies and drilling of oceanic crust indicate that this portion of the crust is composed of a layer of extrusive pillow and massive basalts overlying a layer of sheeted dikes (each 0.5–1.5 km thick) and a transition zone to deeper gabbros (Christensen and Salisbury, 1975; Spudich and Orcutt, 1980a, 1980b; Anderson et al., 1982). Cracks, fissures, and cavities between pillows in the extrusive layer increase porosity and reduce seismic velocity. A large portion of the increase in seismic velocity with depth may be due to a decrease in the number and size of voids.

Azimuthal anisotropy of ±0.2–0.5 km/s in upper oceanic crust has been demonstrated on the basis of *P*-wave arrival times (White and Whitmarsh, 1984; Shearer and Orcutt, 1985; Little and Stephen, 1985) and particle motions of *S*-waves (Stephen, 1981, 1985). Different periods of variation have been found (90°—White and Whitmarsh, 1984; 180°—Shearer and Orcutt, 1985; Little and Stephen, 1985); however, the phase of variation has always been linked to the paleospreading direction. Shearer and Orcutt (1985) and Stephen (1985) argue that fluid-filled cracks oriented perpendicular to the spreading direction, rather than dry cracks or a layered velocity structure, produce the observed 2θ velocity variations. White and Whitmarsh (1984) argue that such a model should produce 4θ variations in velocity.

To try to resolve seismic structure on these scales, an OSE was conducted during ODP Leg 102 at Hole 418A (110 Ma, magnetic anomaly *M0*) in the western North Atlantic (Fig. 1). Basement penetration at Hole 418A (544 m) was deeper than any other hole in crust older than 7 Ma (Hole 395A). Substantial information was already known about this site and nearby (~7.5 km) Site 417 from drilling, logging, and an an OSE in Hole 417D (Donnelly, Francheteau, et al., 1980). The drilled section at Holes 418A and 417D is predominantly pillow basalt with smectite infilling, breccias, and massive basaltic sills or flows; minor dikes occur ~0.5 km below top of basement. Laboratory-measured velocities range from 4.0 to 6.7 km/s (Christensen et al., 1980). Bulk-rock velocity varies ±1 km/s (or 20%) over a centimeter scale. Sonic logs (sensor spacing of 0.6 m) at Hole 417D obtained velocities systematically lower than lab measurements on basalts due to integration of crack porosity and low-velocity void infilling by smectite within the basalt (Salisbury et al., 1980b). *P*-wave velocities measured on lab samples from upper portions of nearby Hole 417A are ~0.5 km/s slower than those in the equivalent section ~0.45 km away at Hole 417D, which indicates a minimum horizontal velocity gradient of ~1 s^{-1}. The velocity difference is attributed to alteration at Hole 417A by seawater circulating through an originally sedi-

[1] Salisbury, M. H., Scott, J. H., et al., 1988. *Proc. ODP, Sci. Results*, 102: College Station, TX: (Ocean Drilling Program).
[2] Address: Woods Hole Oceanographic Institution, Woods Hole, MA 02543.

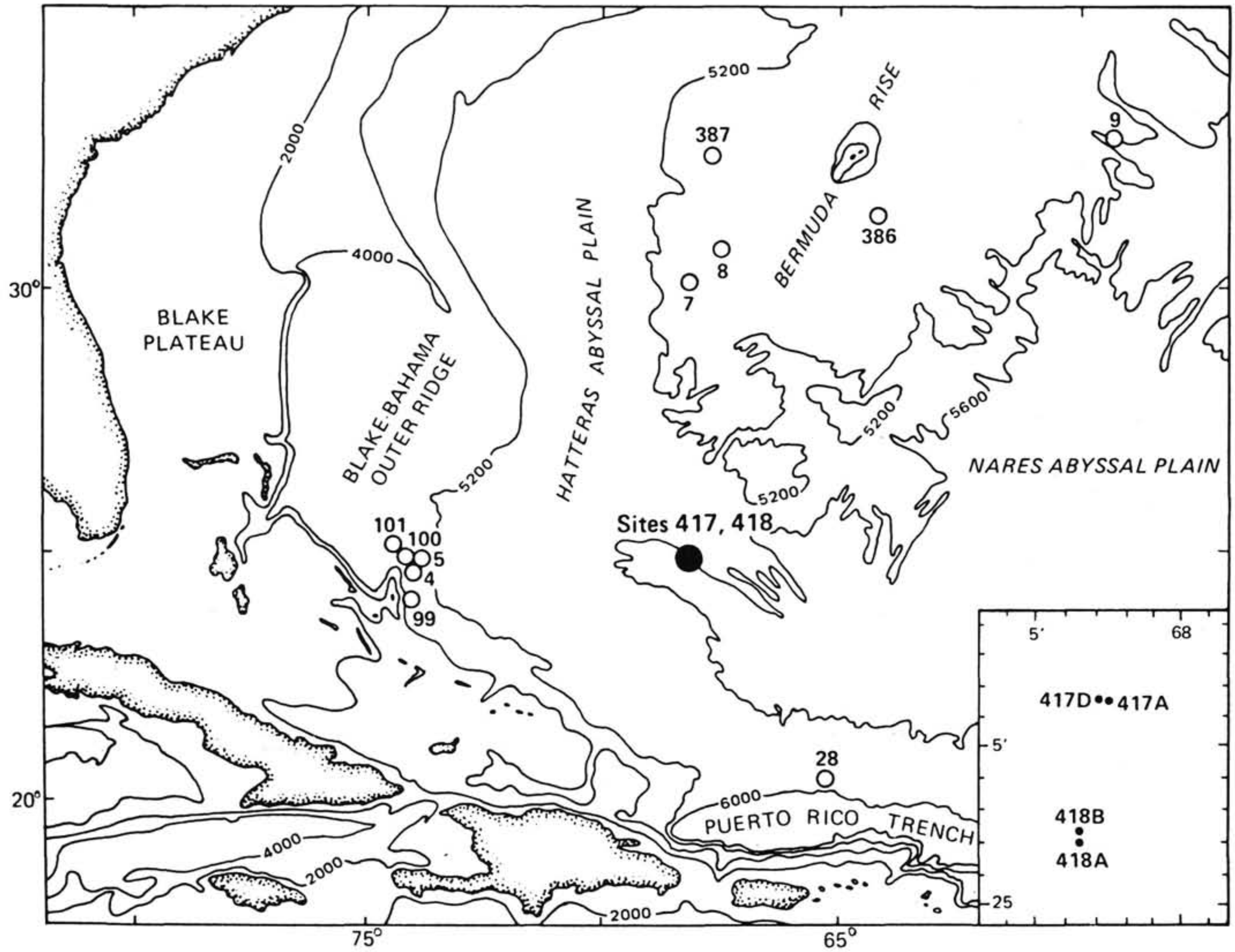

Figure 1. Location of Hole 418A from Donnelly, Francheteau, et al. (1980). Bathymetry in meters.

ment-free basement high (Donnelly et al., 1980; Salisbury et al., 1980b).

Hole 417D OSE velocities obtained by amplitude analysis (Stephen et al., 1980) and inversion of P-wave arrivals (Stephen and Harding, 1983) agree well with an average velocity of ~4.8 km/s from logging (Salisbury et al., 1980a). The inversion results suggest a downward decrease in velocity gradient from 2.3 s^{-1} above ~1 km to ~1.0 s^{-1} between 1 and 1.5 km.

In this paper we report velocity-depth analysis of P-wave arrival times from shots on radial lines by the τ-ζ inversion method (Dorman and Jacobson, 1981; Stephen and Harding, 1983) and anisotropy analysis by Fourier decomposition of arrivals from shots on circular lines. We describe in detail the reduction of these data because this information is critical to evaluating our results and assessing agreement with future studies of the data set.

FIELD METHODS

For this study a triaxial seismometer was clamped at 430, 330, 230, 81, and 41 m below the sediment/basement contact (Fig. 2). After amplification, the voltage signal from the seismometer was sent via coaxial cable to the Masscomp computer in the underway geophysics laboratory aboard the drillship *JOIDES Resolution*. The signal was digitized at 500 Hz for 20 s and recorded on magnetic tape. Digitization began 3 s after receiving a field break signal via radio from the shooting ship. Seismograms are presented in the appendix to the Site 418 report (Shipboard Scientific Party, 1986).

The R/V *Fred H. Moore* made 3296 shots oriented along radial lines and circles about the drill hole. Figure 3 shows locations of all shots for which traveltimes were picked. Locations of individual lines are shown in the Site 418 report (Shipboard Scientific Party, 1986). Explosive charges (15-30 1b Tovex) were shot at 3-min intervals while moving at ~6 kt, giving shot spacings of ~0.5 km. The shooting pattern for explosives included radial lines at ranges of 4-10 km and circles at 6- and 8-km ranges. The *Moore* air gun array (1-2 2000-in.^{3} guns operated at 2000 psi and a tow depth of ~9 m) was fired every 1 min at speeds of 3-6 kt to give shot spacings of 0.1-0.2 km. Radial air gun lines ranged from 0.5 to 2 km and, rarely, from 0.5 to 8 km (lines 1-6 at seismometer depth 330 m, shots 1011-1282 and 1724-1852). Circles were shot with air guns at radii of 2 and 4 km.

Aboard the *Moore* shot times were detected by monitoring a blast phone on the air gun array during air gun shooting and a hydrophone trailed behind the ship during explosive shooting. Shot detection triggered radio transmission of the coded field break signal to the recording system aboard the drillship.

Range and azimuth from shot to borehole receiver were calculated during initial post-cruise data reduction from the range

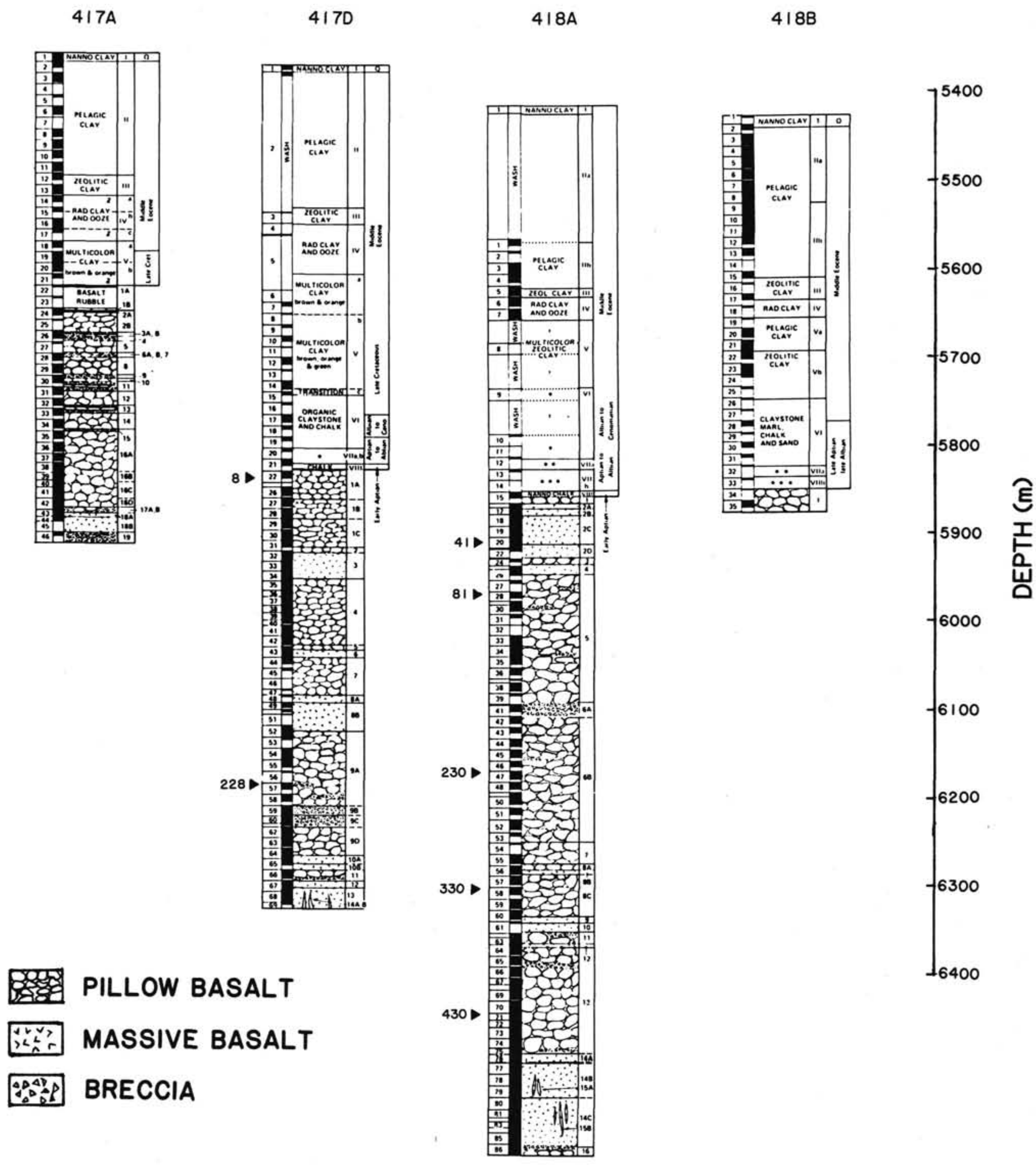

Figure 2. Borehole stratigraphy at Sites 417 and 418 from Donnelly, Francheteau, et al. (1980). Scale at right is depth in meters below sea level. Arrowheads and boldface numbers indicate depths (m) below the sediment/basement contact at which OSE seismometer was clamped during Leg 53 (Hole 417D) and Leg 102 (Hole 418A).

and bearing recorded during the experiment between ships and from the position of the borehole (25°02.10′N, 68°03.44′W; Donnelly, Francheteau, et al., 1980). Range and bearing between the shooting location and the drillship were measured for each shot by calibrated Del Norte transponders placed on the bow and stern of the *Resolution* and the bridge of the *Moore*. These fixes, corrected for the shot location behind the *Moore* and for the center of the drilling rig, were accurate to ± 10 m.

Errors in range, however, occurred because the drillship was not positioned directly over the hole and thus, not directly over the receiver, and because the drillship moved with respect to the hole during the experiment. Due to flexing of the pipe string,

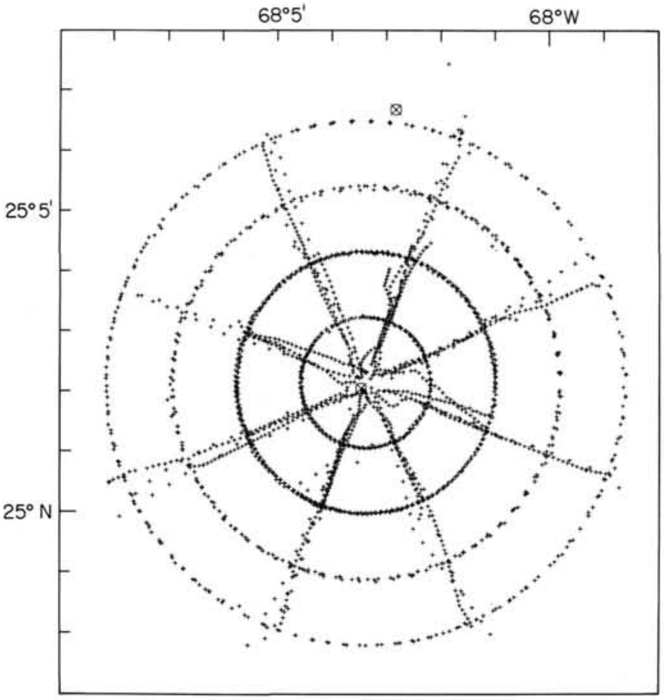

Figure 3. OSE shot locations. Crosses mark all shots at all seismometer depths for which traveltimes were picked. Circled X's indicate Holes 417D (edge) and 418A (center).

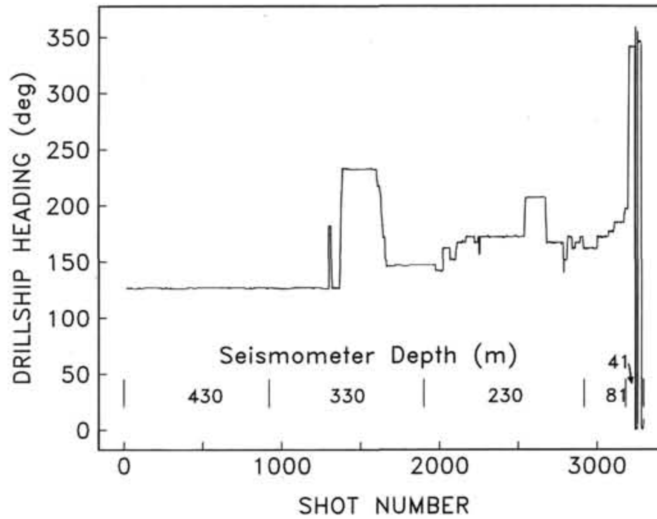

Figure 4. Heading of *JOIDES Resolution* as a function of OSE shot number.

the horizontal distance between the drilling rig and the hole in the seafloor may vary during normal operating conditions by up to 5% of the water depth. Thus, pipe flexing at Hole 418A could lead to errors of up to 0.25 km. Furthermore, problems with software and the placement of dynamic-positioning transducers aboard *Resolution* caused the dynamic-positioning system to move the drillship whenever the heading was changed to adjust for changing wind and swell conditions. Unfortunately, transit satellite fixes were not recorded on the drillship during shooting, so the location of the drillship relative to the hole is uncertain. That an offset actually occurred was verified during initial reduction of data from the 430-m seismometer location. Fourier functions fit to *P*-wave traveltimes (method described subsequently) showed a consistent 1θ variation of ± 0.03 s, with later arrivals from N52°E. These data indicated that the drillship was northeast of the hole. During OSE operations, the drillship made infrequent, episodic bearing changes of several tens of degrees (Fig. 4). However, sufficient information about the geometry of the drillship's transducers could not be obtained to calculate resultant changes in drillship position.

In an attempt to correct this source of range error, the position of the drillship was calculated using the satellite positions of the *Moore* and the relation of the *Moore* to the drillship. The location of the *Moore* was determined by transit satellite fixes recorded when available throughout the experiment. The event times of all 73 satellite fixes recorded on the *Moore* during shooting were compared with shot times. For 65 fixes the difference in time between a fix and a shot was less than 0.5 min. For each of these fixes, a shot position was found by linear interpolation for the exact time the satellite fix was made. These positions were relocated to the satellite receiver on the *Moore*. The satellite logs were reexamined, and 21 of the satellite fixes were judged to be of poor quality (large standard deviations in latitude and longitude) due principally to adverse satellite elevations ($<20°$ or $>70°$ above the horizon). Table 1 gives the remaining 44 pairs of locations of the *Moore* from satellite navigation and from range and bearing to the static hole location. The difference between these positions is an estimate of the offset of the drillship from the borehole. Figure 5 shows the calculated location of the drillship with respect to the position of Hole 418A. Using Figure 4, we determined those shots when the drillship heading and, presumably, the drillship-to-hole distance remained constant. The average offset between drillship and hole during these periods is given in Table 2 and plotted in Figure 5. Because the standard deviations in these offsets overlapped, the data were judged too imprecise to detect systematic movement of the drillship during the course of the experiment. In order to remove at least a portion of the error due to offset of the drillship from the hole, the average of all 44 offsets (0.210 km at N40.3°E; Table 2) was used to recalculate the position of each shot in the experiment.

In general, the signal-to-noise character of records from all three geophones was excellent. The only persistent degradation of signal occurred while the seismometer was locked at 330 m. In the return from the vertical geophone, noise at 30–35 Hz obscures fine waveform features but not the general character of the signal. The noise began during air gun operations at shot 1563 in the 4-km circle and continued through the 2-km circle and radial lines 5 (ESE), 6 (ENE), and 7 (WSW) to the end of shooting at that seismometer depth (shot 1899). In addition, the signal from one of the horizontal geophones (H2) is degraded by episodic, high-amplitude events. These events occur throughout air gun shooting at 330 m, but the frequency and amplitude of events is markedly higher between shot 1724 and the end of shooting at this depth (shot 1899). For these shots (radial lines 5, 6, and 7) the quality of H2 data is very poor.

DATA REDUCTION

The object of this study was an analysis of *P*-wave traveltimes using inversion and Fourier decomposition techniques already developed for OSEs (Stephen and Harding, 1983; Little and Stephen; 1985). These techniques require that picks of *P*-wave traveltime along radial and circular shot patterns be reduced to the top of oceanic basement by subtracting the traveltime through water and sediment. Thus, the seismograms collected in this study were processed in three steps: (1) traveltime corrections, (2) picking arrival times, and (3) reduction to basement.

Table 1. Comparison of simultaneous fixes for *Moore* from transit satellite and from range and bearing to *Resolution* (using hole location from Donnelly, Francheteau, et al., 1980).

Closest shot	Satellite fix						Range and bearing	
	Latitude	Longitude	Julian day	Hr	Min	S	Latitude	Longitude
112	24.9659°	68.0170°	90	10	10	48	24°57.987′	68°1.042′
144	25.0652°	67.9985°	90	11	59	12	25°4.032′	67°59.814′
165	25.0981°	68.0964°	90	13	8	48	25°5.903′	68°5.782′
187	25.0009°	68.1278°	90	14	14	0	25°0.049′	68°7.464′
200	24.9638°	68.0727°	90	14	54	48	24°57.951′	68°4.334′
221	25.0076°	67.9844°	90	15	56	24	25°0.584′	67°59.103′
234	25.0830°	68.0321°	90	16	56	24	25°5.092′	68°1.814′
250	25.0512°	68.1147°	90	17	45	12	25°3.137′	68°6.921′
361	25.0205°	68.0636°	90	22	14	48	25°1.367′	68°3.764′
469	25.0466°	68.0878°	91	0	3	12	25°2.774′	68°5.258′
484	25.0373°	68.0655°	91	0	18	0	25°2.388′	68°3.850′
515	25.0221°	68.0217°	91	0	49	12	25°1.383′	68°1.212′
590	25.0268°	68.0758°	91	2	4	24	25°1.691′	68°4.514′
619	25.0106°	68.1288°	91	2	34	0	25°0.675′	68°7.636′
892	25.0210°	68.0708°	91	7	5	36	25°1.284′	68°4.178′
1114	25.0713°	68.0438°	91	11	36	48	25°4.357′	68°2.574′
1310	25.1033°	68.0318°	91	16	6	24	25°6.280′	68°1.910′
1346	24.9856°	68.1160°	91	17	54	0	24°59.232′	68°6.831′
1372	24.9924°	67.9933°	91	19	12	24	24°59.718′	67°59.489′
1419	25.0046°	68.1064°	91	21	52	0	25°0.252′	68°6.239′
1527	24.9992°	68.0527°	92	1	26	0	24°59.974′	68°3.084′
1679	25.0516°	68.0498°	92	3	57	36	25°3.155′	68°2.991′
1737	25.0282°	68.0380°	92	4	56	0	25°1.790′	68°2.129′
1784	25.0240°	67.9793°	92	5	43	12	25°1.458′	67°58.724′
1844	25.0423°	68.0391°	92	6	43	12	25°2.640′	68°2.281′
1979	25.0532°	67.9811°	92	11	14	24	25°3.288′	67°58.804′
2040	24.9809°	68.0575°	92	14	22	0	24°58.942′	68°3.255′
2059	25.0539°	68.0020°	92	15	17	36	25°3.250′	68°0.008′
2093	25.0162°	68.1136°	92	17	0	0	25°0.997′	68°6.698′
2116	25.0182°	68.0484°	92	18	48	0	25°1.210′	68°2.802′
2164	25.1006°	68.0270°	92	21	28	48	25°6.138′	68°1.393′
2216	25.0197°	68.0995°	93	0	17	36	25°1.168′	68°5.862′
2247	24.9864°	68.0325°	93	2	2	0	24°59.241′	68°1.746′
2280	25.0434°	68.0754°	93	3	8	24	25°2.609′	68°4.415′
2472	25.0458°	68.0197°	93	6	21	12	25°2.847′	68°1.084′
2797	25.0273°	68.0530°	93	11	46	24	25°1.666′	68°3.017′
2884	25.0365°	68.0546°	93	13	13	12	25°2.228′	68°3.135′
2905	25.0295°	68.0317°	93	13	34	0	25°1.871′	68°1.823′
2963	25.0371°	68.0597°	93	14	59	12	25°2.286′	68°3.495′
3038	25.0125°	68.0257°	93	16	14	0	25°0.863′	68°1.316′
3061	25.0366°	68.0405°	93	16	36	48	25°2.288′	68°2.543′
3231	24.9846°	68.0806°	94	0	53	36	24°59.141′	68°4.509′
3252	25.0807°	68.0268°	94	2	38	48	25°5.161′	68°1.418′
3275	25.0668°	68.0448°	94	4	3	12	25°4.066′	68°2.493′

Time Corrections

At sea, the data-logging system aboard the *Resolution* assumed that shot time was the field break time, at which a coded radio signal arrived from the *Moore*. The only consistent sources that sum to greater than a millisecond of time lag between the shot and triggering of the recording system are the flight time from explosive to the shot-detection hydrophone and the encoding-decoding of the radio signal. The flight-time correction for explosives was calculated following Stephen et al. (1980). A delay of 39 ms ± 5 ms in the radio transmission system was measured in the lab and applied to all shot times.

We checked our timing method against two independent sets of timing data. Shot times were also logged on the *Moore*. Shot times from the *Moore* and from the data-logging system on the drillship were corrected using drift rates measured against a satellite time standard and compared. In addition, analog tapes were made on the drillship of the seismometer signal against a clock that was independent of the digital data-logging system. Arrival times for the same seismic event (e.g., *P*-wave arrival) were determined using both digital and analog systems and compared. These checks indicated a consistent error throughout the experiment of ~0.25 s in our shot time. The source of this error was located in the logic of the field break detection by the recording system on the drillship. During the experiment, the recording system triggered on the trailing edge of a voltage pulse from the radio signal decoder instead of the leading edge. We measured the pulse width as 0.242 s, with a standard error of <0.005 s, and applied this correction to all shot times.

Picking Arrival Times

After static timing corrections were applied, seismograms from 2444 shots sorted into radial lines and circles were available for picking. Compressional- and shear-wave arrivals were picked on 2213 shots. Because the density of shots along lines is high, traveltimes were not picked for shots with significantly degraded signal-to-noise ratios and ambiguous first arrivals. *P*- and *S*-wave arrival times from the air gun source could be picked reliably out to 8 km, the range limit of our experiment. *S*-waves could be traced on some air gun lines as a low-amplitude phase to shots within ~0.5 km of the receiver. Figure 6 shows seismograms from a representative air gun line with shots between 0.5 and 4 km. The seismograms for the horizontal 2 and vertical geophones at ranges of 1–4 km have *S*-wave amplitudes much greater than those of *P*-waves. At ranges less than 1 km, ray ori-

Table 2. Average offset of drillship from position of Hole 418A during periods of constant drillship heading. Numbers in parentheses are standard deviations.

Shot number			Offset				
Start	End	Ship heading	Latitude (min)	Longitude (min)	Range (km)	Bearing	Number of fixes
0	1360	130°	0.07308	0.05755	0.166	36°	23
1640	2010		(0.04866)	(0.06072)			
2010	2540	165°	0.03720	0.1020	0.185	68°	15
2670	3170		(0.1130)	(0.1177)			
1360	1640	230°	0.05800	0.1100	0.214	60°	3
			(0.1033)	(0.03305)			
3170	End	360°	0.1480	0.2380	0.483	56°	3
			(0.1472)	(0.07452)			
		All	0.07362	0.09534	0.210	40°	44
			(0.06096)	(0.08484)			

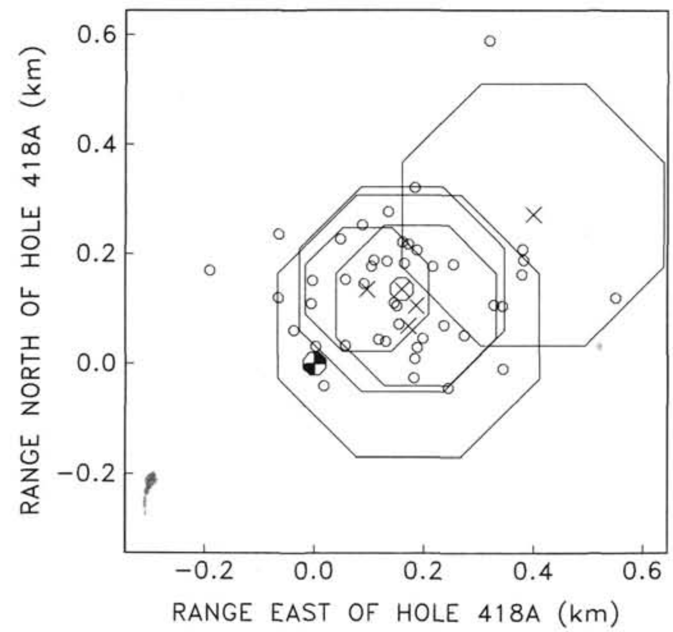

Figure 5. Position of drillship relative to Hole 418A position. Hole 418A marked by partially shaded circle. Small circles indicate the positions of drillship determined from all high-quality satellite fixes received on the *Moore* and from the relation of the *Moore* to the drillship, as determined by Del Norte transponders. The average of all offsets is marked by an X within a circle. Other X's mark offsets averaged over periods of constant ship heading (Table 2). The radii of the octagons centered on X's are the standard deviations of the average offsets.

entation becomes close to vertical, and, presumably, less compressional-wave energy is converted to shear energy (White and Stephen, 1980). Thus, the amplitudes of *P*- and *S*-wave arrivals are more nearly equivalent. The horizontal 2 geophone is oriented close to the azimuth of the shooting line, so the *S*-wave is weak.

Traveltime picks have a measurement precision of ±0.004 s. Sources of larger traveltime error include noise obscuring a first arrival, judgment in recognizing a first arrival, and receiver bandwidth (Kennett and Orcutt, 1976; Bratt and Purdy, 1984). Bratt and Purdy (1984) estimated these errors to be ±0.030–0.150 s (95% confidence interval) for seafloor receivers with explosion sources. For borehole data, we estimate a significantly lower picking error, ±0.010–0.050 s, because of the much better coupling, higher signal-to-noise ratio character of our data, and the bandwidth of our receiver (4.5–100 Hz).

Arrival times sometimes differ among the three channels by up to 0.02–0.04 s (Fig. 7). Which channel receives the earliest arrival depends systematically on the range and azimuth of the shot. The differences are generally consistent with interpreted changes in the direction of the particle motion with respect to the triaxial seismometer. During picking of both *P*- and *S*-wave arrivals, all three channels were usually scanned to assure that the earliest arrival was found. Commonly, arrivals were picked on more than one channel. For traveltime analysis, only the earliest arrivals were used, regardless of the channel picked.

Reduction to Basement

Traveltimes were reduced to the top of basement by subtracting the time for passage through water and sediment following the water-path correction method of Purdy (1982). This method finds the ray path length through water and sediment from the horizontal slowness ($p = (\sin i)/V_i$) and the thickness of water and sediment at the ray entry point. The method makes no assumptions about basement velocity structure and has errors of 0.01–0.03 s due to uncertainties in estimating slowness, water depth, and sediment thickness (Purdy, 1982; Bratt and Purdy, 1984).

For a buried receiver, horizontal slowness is low near the receiver, increases to a maximum at the range from which rays travel horizontally into the receiver, and then decreases with range (Stephen and Harding, 1983; Little and Stephen, 1985). In this experiment, horizontal slowness was estimated for each seismometer depth as a function of distance by differentiating a curve fitted to traveltimes of shots made on radial lines ($p = dT/dX$). The traveltime-range (T-X) data were fit with a cubic spline by a least-squares method. Locations of knots (ranges between which the T-X data are fit with a cubic polynomial) were adjusted by trial and error to obtain a single inflection point. Data shot on circles were not used because the resultant fit would be unduly weighted at those ranges. Figure 8 shows the final fits plotted with all T-X data.

This method is sensitive to outliers and to the tails of the distribution. Up to 17 shots at ranges much greater than the inflection point had to be excluded in order to get a fit with one inflection point. Arrival times for these shots were up to 0.160 s earlier than those for most shots at these ranges. These shots were all located to the east of the drill site over seafloor up to 150 m shallower than the regional average (Senske and Stephen, this volume). Table 3 gives the number of shots used to get a fit, inflection point ranges, and rms error for each seismometer depth.

Traveltime corrections were calculated assuming velocities of 1.516 km/s in water and 1.8 km/s in sediment. The assumed sediment velocity is higher than most lab measurements (Donnelly, Francheteau, et al., 1980) but close to a depth average of sonic velocities logged at Hole 417D (Salisbury et al., 1980a). The seafloor over the site slopes gently westward (Senske and Stephen, this volume), so water depth at the ray entry point was found by linear interpolation between the depth beneath the shot and the depth at Hole 418A (5511 m).

We assumed that sediment thickness was equivalent everywhere to that drilled at Hole 418A: 324 m (Donnelly, Francheteau, et al., 1980). Because the seismic-reflection survey indicates that sediment thickness varies over a range of 0.2–0.4 km (Senske and Stephen, this volume), this assumption introduces errors of up to ±0.05 s into our corrected traveltimes. Analog profiles made on the *Moore* during air gun shooting were not used because the quality of records was poor; as a result, basement was difficult to resolve. We tried a τ-ζ inversion of *P*-wave picks that had been reduced to basement using bathymetry and depth to basement digitized from the maps of Senske and Stephen (this volume). Traveltimes calculated by ray tracing through

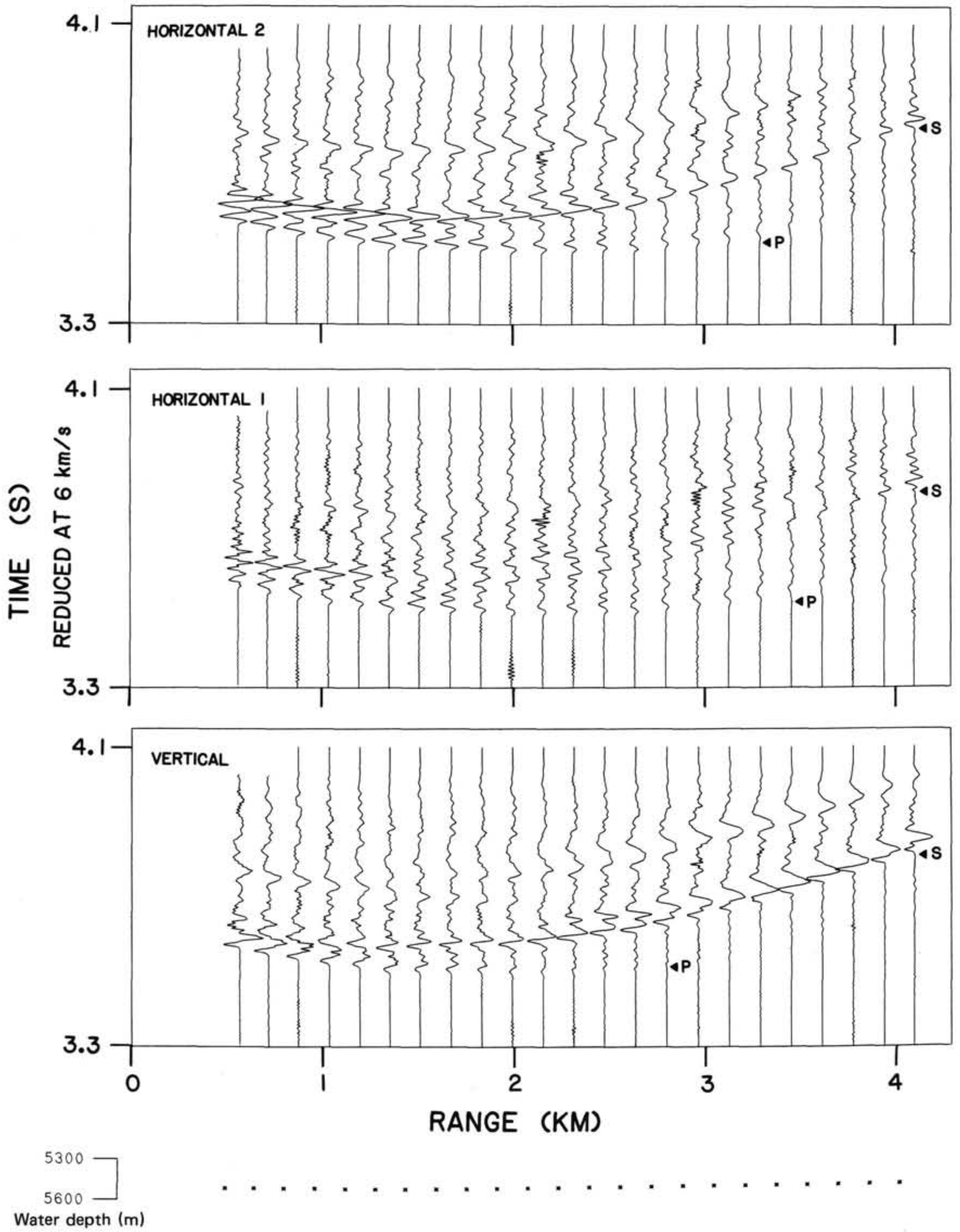

Figure 6. Seismograms and water depth along a radial line. Note *S*-wave arrivals at shot ranges of less than 1 km. Seismometer at 230 m. Traces for horizontal geophones are shown in upper two panels; vertical geophone in lower panel. Time reduced at 6 km/s. Line shot with air guns at a bearing of ~60°. Amplitude of seismograms scaled by range according to $A(X^4/4)$, where A is a linear scaling factor and X is range (km). The scale factor (A) for the horizontal 2 geophone is twice that of the other geophones. Seismograms were low-pass filtered with a roll off between 120 and 145 Hz.

this velocity model (Fig. 9A) are significantly later than the observed arrivals (Fig. 9B). Apparently, correcting traveltimes using these maps introduces systematic variation of sufficient magnitude to distort the gross averaging of vertical velocity structure done by the τ-ζ technique, whereas the assumption of a constant sediment thickness introduces errors that are more nearly random. The systematic variation may be caused by lateral variation in crustal velocity or by errors in the maps. The primary source of error in the depth-to-basement map is the inability of reflection seismology using surface-towed gear to adequately resolve the true form of basement features. For example, note the poor resolution of basement near Site 417 in Figure 7 of Senske

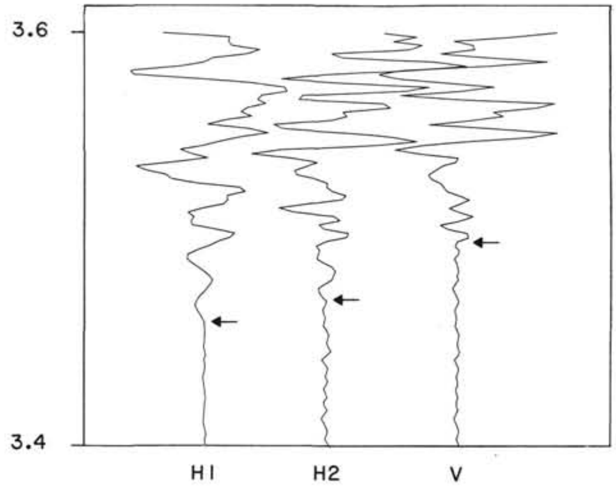

Figure 7. Detail of unfiltered seismograms showing apparent difference in *P*-wave arrival time (arrows) on different geophones (H1, H2, and V) for one shot. Time reduced at 6 km/s. Shot 55 (Tovex) at 3.134-km range and a bearing of 292° with seismometer at 430 m. Same amplitude scaling for each geophone.

and Stephen (this volume) and the large difference between Holes 417A and 417D in depth to basement measured by drilling (0.13 km, Fig. 2), which is not shown on the map.

To reduce arrivals from shots made on circles, we used horizontal slowness vs. range functions estimated from the radial-line data. The ranges of all shots on each circle were averaged, and time was added to or subtracted from each arrival time to move the shot to the average range along the curve fit to radial T-X data at the same seismometer depth. The horizontal slowness of all shots on the circle is, thus, equivalent to the slope of the radial T-X curve at the average range (Table 4). At the 81-m seismometer depth, radial lines were not shot far enough to intercept the 6- and 8-km circles, so the T-X relationship at 230 m was used for these circles.

Figure 10 shows the reduced T-X plot for all seismometer depths. These data were again fit with a cubic spline following the procedure described previously except that it was not necessary to exclude any shots to get fits with a single inflection point.

VELOCITY ANALYSIS

Inflection Point Analysis

For a buried receiver in a laterally homogeneous medium where velocity increases monotonically with depth, the slope of the T-X curve (horizontal slowness) at the inflection point is the reciprocal of the interval velocity at the receiver depth (Gutenberg, 1953; Stephen and Harding, 1983; Little and Stephen, 1985). Stephen and Harding (1983) weighted their estimates of slowness at the inflection point with values at adjacent ranges. For this experiment, the maximum slope of the cubic spline, which is always at the inflection point, was taken as the inverse velocity at the receiver depth. As a result, the velocity is sensitive to the curve-fitting procedure and is probably not accurate to better than ± 0.2 km/s. Curves fit to traveltime data before reduction to basement (Table 3) yield velocities 0.25–0.35 km/s higher than velocities from fits to data after reduction. Such misfit was not found in earlier OSEs (Little and Stephen, 1985). We attribute the discrepancy here to the curve-fitting procedure and to unknown violations of assumptions in removing traveltime through water and sediments.

Velocity Inversion

Dorman and Jacobson (1981) proposed a method of inverting T-X data to a velocity-depth function. The method assumes flat, laterally homogeneous velocity structure with linear velocity gradients within layers and no velocity discontinuities at layer bounds. Data are first transformed to two new parameters:

$$\tau(p) = T - pX$$

$$\zeta(p) = T + pX$$

These data are grouped by range using an optimization routine that seeks segments having minimum variance of τ and ζ. The thickness represented by each segment is found by a linear inversion method. A velocity-depth function can be found by downward integration from an assumed surface velocity.

Stephen and Harding (1983) adopted the τ-ζ method for use with OSE data. Little and Stephen (1985) showed that inverse solutions found by this method at Hole 504B agree well with velocities found by inflection point analysis and sonic logging. Synthetic traveltime curves generated by ray tracing through the velocity-depth solution were consistent with the traveltime data. In addition, amplitudes of synthetic seismograms calculated using the reflectivity method and τ-ζ inversion velocities agreed well with record sections.

For this experiment, a cubic-spline function was fit to the T-X data after reduction to basement using only the criteria of minimum least squares and a single inflection point. The function was differentiated twice to give values of slowness (p) and curvature at each shot. The standard error of fit was recalculated on either side of the inflection point and used as a measure of the scatter in τ. Data at the 81-m seismometer depth were not distributed over a broad enough range to resolve an inflection point and give a stable cubic-spline fit, so these data were not used in the τ-ζ inversion.

Following Dorman and Jacobson (1981) and Stephen and Harding (1983), optimal segments were found in branches on both sides of the inflection point, and average values of τ, ζ, and p were calculated for each segment (Table 5). Energy returned from shots beyond the range of the inflection point turns beneath the receiver, so segments found in the far branch represent layers of constant velocity gradient. Three of the six segments found in this branch have significantly different values of average slowness (Table 5; upward-directed rays). Depth to these three slowness values (layer bounds) and their 95% confidence intervals were found by linear inversion and downward integration (Table 6 and Fig. 11). For depth integration, we assumed that the velocity at top of basement (V_{surf}) was 4.545 km/s, the 41-m seismometer inflection point velocity determined on T-X data reduced using bathymetry and depth to basement digitized from maps in Senske and Stephen (this volume). Varying V_{surf} between 4 and 5 km/s had little effect on depth to deeper layer bounds (Fig. 12).

To check our inversion results we made two forward models of the data. In the first model, traveltime curves were calculated by ray tracing from the inversion velocity-depth profile, assuming flat, laterally homogeneous layers with constant velocity gradients. These curves are in good agreement with the T-X data. In Figure 13, the traveltime curve for a receiver at 430 m is compared with observed T-X data. The curve fits most data. Between 1 to 2.5 km, however, the modeled arrival times offset the cubic-spline fit to the data by ~ 0.035 s. Velocities above the receiver control traveltime at these ranges. The misfit suggests that our assumed surface velocity may be 0.1 to 0.2 km/s too low.

The second model compares the range-amplitude relations in our data with those of full-waveform synthetic seismograms cal-

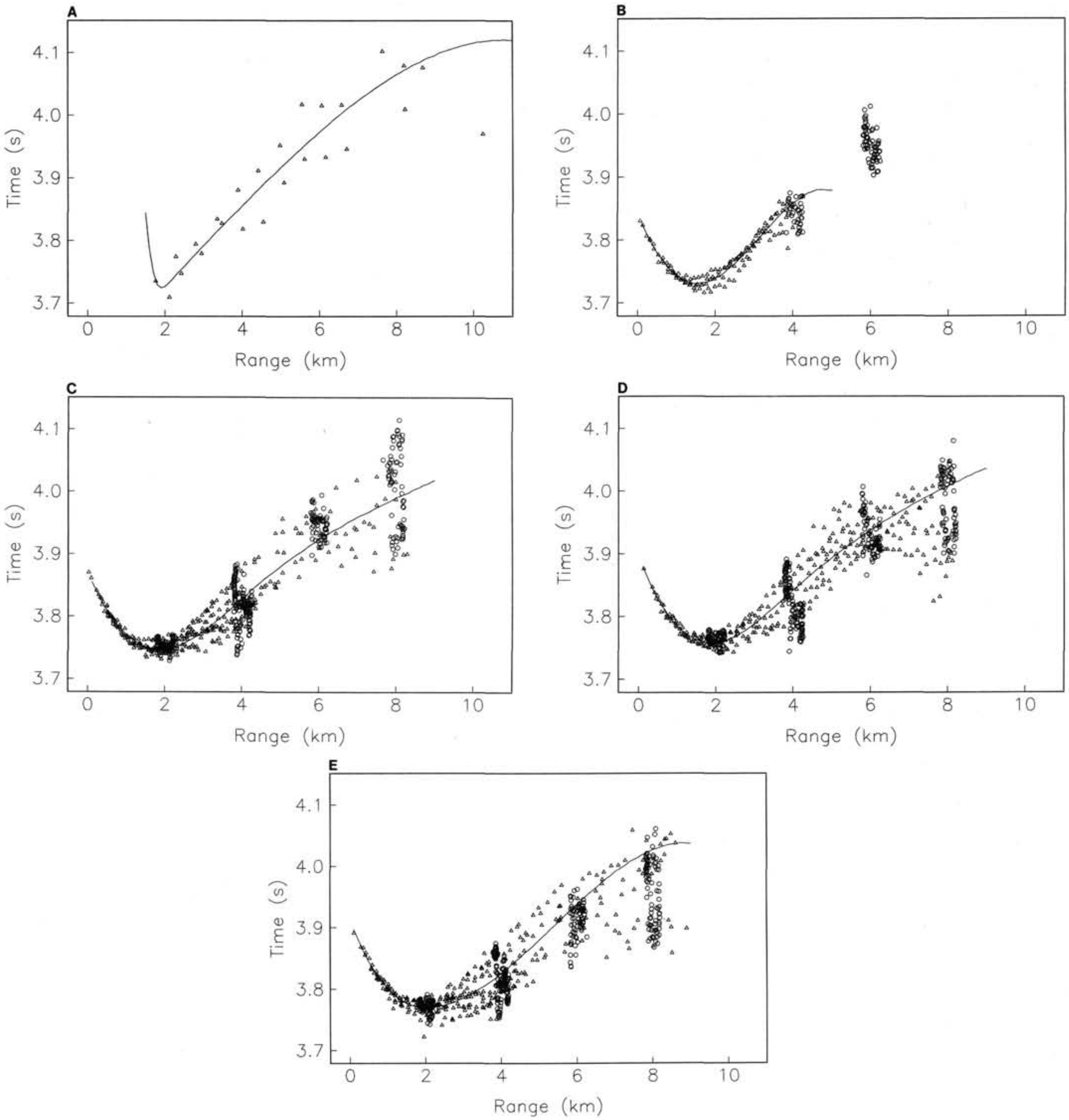

Figure 8. T-X plot of *P*-wave first arrivals before reduction to basement. Time reduced at 6 km/s. Triangles indicate arrivals from shots on radial lines; circles indicate arrivals from circles. Line is cubic-spline fit to radial line data only. Seismometer at (A) 41, (B) 81, (C) 230, (D) 330, and (E) 430 m.

culated from the τ-ζ inversion results using the reflectivity method (Fuchs and Müller, 1971; Stephen, 1977). A V_s/V_p ratio of 0.55 (Poisson's ratio = 0.28, from table 4 of Birch, 1961), suggested by preliminary fits to the *S*-wave arrival times, was used to determine an *S*-wave velocity-depth profile. Velocities and densities used in the calculations are presented in Table 7 and Figure 14. Peak power of the source function used in modeling was between 1 and 10 Hz. Seismograms were calculated for a vertical geophone and for a geophone oriented horizontally along the axis of the shooting line. Figure 15 shows reflectivity and observed seismograms for vertical and horizontal geophones as a function of range at each geophone depth. The seismograms are overlain by smooth traces through our picks of *P*- and *S*-wave arrivals. In selecting data for illustration, we tried to be consistent as to line azimuth, to find good quality data with broad range coverage, and to match the amplitude patterns

Table 3. Inflection point velocities from fits to radial line data.

Geophone depth (m)	Data processing	Number of shots fit	Rms error (s)	Inflection point range (km)	Velocity (km/s)
41	Before reduction	24	0.0362	2.43	4.71
	[a]After reduction	24	0.0496	—	5.09
81	Before reduction	119	0.0098	3.18	4.63
	After reduction	—	—	—	—
230	Before reduction	294	0.0212	3.95	4.92
	After reduction	302	0.0234	2.45	4.67
330	Before reduction	245	0.0198	3.73	4.93
	After reduction	284	0.0224	2.35	4.59
430	Before reduction	305	0.0315	4.55	5.03
	After reduction	305	0.0236	2.59	4.79

[a] Straight line fit.

in the synthetic seismograms. It is reasonable to be selective in choosing which of the 2 to 8 azimuthal lines at each seismometer depth are to be used for comparison because the orientation of the horizontal geophones varied among geophone depths and because significant amplitude variations occur due to real lateral variations in velocity structure and basement topography that are unaccounted for in our model calculations.

For the three deepest seismometer locations at ranges beyond 4 km, a discrepancy occurs between synthetic and observed seismograms. In the synthetics, the amplitude of the first 0.1–0.2 s of the *P*-wave arrival is much lower on the vertical geophone than on the horizontal geophone, whereas in the observed data the difference in amplitude is not as dramatic. Because the *P*-wave angle of incidence from these ranges is nearly horizontal on the receiver, the particle motion is principally horizontal. As a result, the amplitude of the vertical component in the synthetic seismograms is small in comparison to the horizontal (Stephen et al., 1980). Energy observed from the vertical component in the data is probably due to scattering within the basement.

In general, the synthetics agree with the observed seismograms. Our criteria are (1) the relative energy in *P*- and *S*-waves, (2) the range-amplitude relationship of the *S*-wave, and (3) the relative energy from the vertical and horizontal geophones. Synthetics and observed data differ primarily in the range-amplitude relationships of the *S*-waves. Because we were able to find at least one line in good agreement, we are confident that the τ-ζ velocity profile represents the "average" velocity structure within ~6 km of Hole 418A. The variance in amplitude among the observed *S*-wave arrivals may indicate lateral variability in either the *P*-wave velocities, which is smoothed by the τ-ζ inversion method, or in the ratio of *P*- to *S*-wave velocities.

Interval Velocities

Energy from a shot fired close to the drillship presumably follows a near-vertical path to the borehole receiver. Assuming that the ray path is vertical and linear, average velocities for depth intervals between receiver clamping locations can be estimated from differences in arrival times. Table 8 and Figure 11 show interval velocities calculated for *P*-wave arrivals at Hole 418A. We used only air gun shots at ranges between 20 and 175 m (ranges include correction for the offset between drillship and hole). Interval velocity between the sediment/basement contact and 41 m depth was determined from traveltime to the 41-m receiver (range of 117 m) after reduction to basement by the water-path correction method described previously. The results have uncertainties of up to 1 km/s because the traveltime differences (0.015–0.030 s) are the same magnitude as our picking error (±0.010–0.050 s). Overall, the results are in fair agreement with velocities determined by the inflection point and τ-ζ inversion methods.

Discussion

The slope of the velocity-depth model at depths less than 500 m agrees well with inflection point velocities determined on T-X data before reduction to basement (Fig. 11). This agreement supports our assumption that velocity at the top of oceanic basement is 4.5-4.6 km/s. These velocities are at the high end of seismic velocities measured in upper oceanic crust (2–5 km/s) but are well within the range of velocities (4.3–5 km/s) from OSE data gathered at sites with a wide range of crustal ages (1–110 Ma; Stephen and Harding, 1983; Little and Stephen, 1985). Stephen and Harding (1983) argue that the relatively high, uniform velocities are due to sealing effects of sediment cover (~0.1 km) on young crust. Sealed from hydrothermal circulation, the upper crust heats up. Mineralization increases sealing cracks, reducing porosity, and thus, increasing seismic velocity. However, Purdy (1987), using a unique seafloor source and receiver geometry on the Mid-Atlantic Ridge, found that refraction velocity structure beneath a site with no sediment cover was indistinguishable (~4.2 km/s) from that beneath a site of similar age (7 Ma) with ~0.2 km of sediment cover. These results suggest that the relatively high, uniform seismic velocities (4–5 km/s) measured by OSE methods may be characteristic of most upper (0–1 km) oceanic crust over horizontal scales of 10–20 km. Lower velocities (2–3 km/s) may be characteristic only of fracture zones, very young crust, and off-ridge crests, small (less than 10 km) regions of anomalous crust.

Figure 16 compares downhole sonic tool velocities logged on Leg 102 with the velocity-depth function from our τ-ζ inversion. The depth ranges analyzed overlap about 350 m. For the interval as a whole, the average velocity from the sonic log is similar to that from the OSE. By both methods, velocity generally increases with depth, but the gradient measured by the OSE is slightly less than that measured by the logging tool. Salisbury et al. (1980b) found similar results at Hole 417D. They attributed the downhole velocity gradient to a downhole decrease in fractures on a scale less than the sensor spacing of the sonic tool (0.6 m), that is, cracks between pillows and radial cracks within pillows.

The difference in gradient measured by the sonic log and the OSE may reflect a difference between the vertical sequence of lithology sampled at Hole 418A and the average sequence within a distance of 6 km. Massive basalts were cored between the bottom of the log, ~6290 m below sea level (mbsl), and the bottom of the hole (6389 mbsl). The ratio of massive basalt to pillow basalt increases with depth in the hole, so massive basalt may be in greater proportion below the bottom of the hole. Because massive basalts at Hole 418A generally have high velocities (~6 km/s) and low porosities (Salisbury et al., 1980b), the velocity below the deepest log penetration is unlikely to decrease to the velocity-depth trend measured by the OSE. We suggest that downhole velocity gradients measured by the two methods are different because the lithology and/or porosity at Hole 418A is not representative of the local region. On the scale of the OSE (~12 km), either pillow basalts are not as well cemented or massive basalts are not as common as at Hole 418A.

The OSE does not sample velocity fluctuations with depth resolution less than the seismic wavelength (~0.5 km). In the sonic log (Fig. 16), however, vertical velocity gradients occur over shorter distances (0.15–0.2 km). Small deviations of ~0.1 km/s in inflection point velocities from the average τ-ζ trend follow these gradients. This is surprising because we judged the accuracy of these velocities to be no better than ±0.2 km/s. At Hole 504B, inflection point velocities also followed gradients with a scale of one tenth of a kilometer in sonic log velocities (compare figures 9 and 12 in Little and Stephen, 1985).

The OSE results at Hole 418A differ slightly from those at Hole 417D (Fig. 17) but agree well with those at Hole 504B

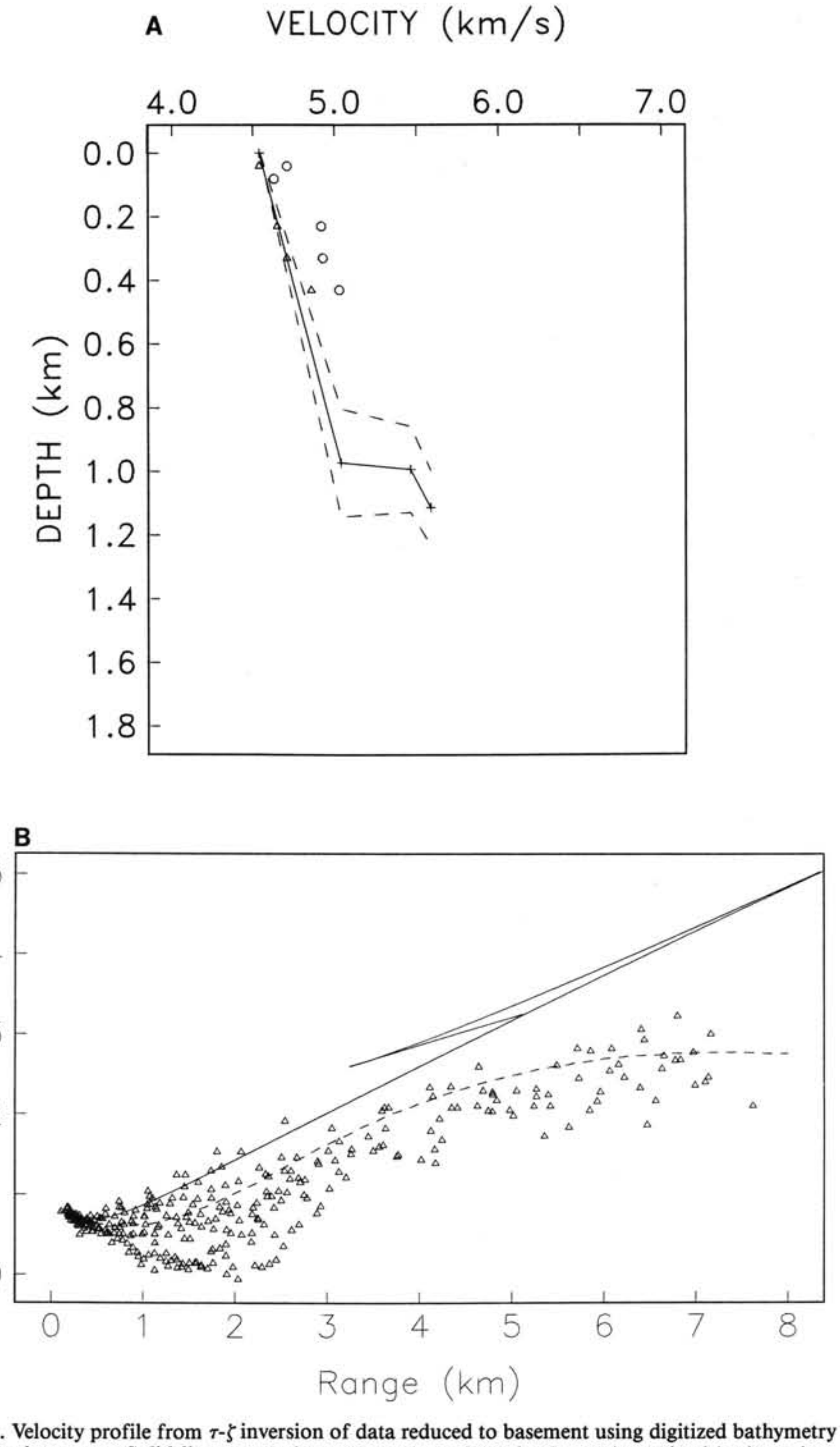

Figure 9. A. Velocity profile from τ-ζ inversion of data reduced to basement using digitized bathymetry and depth to basement. Solid line connecting crosses shows best depths as determined by inversion; dashed lines indicate 95% confidence limits on depths. Circles are inflection point velocities determined on fits to T-X data before reduction to basement (Table 3). Triangles are inflection point velocities from fits to data after reduction to basement. B. T-X data reduced to basement using digitized bathymetry and depth to basement. Time reduced at 6.8 km/s. Solid line connects arrival times calculated by ray tracing using model velocities in Figure 9A with seismometer at 430 m. Dashed line is cubic-spline fit to data.

(Fig. 18). The confidence limits at Hole 417D are broader than those at Hole 418A. This may be due to the considerably larger number of shots and two additional seismometer depths used in the inversion at Hole 418A rather than to a real difference in velocity variability between the sites. The primary difference between the OSE results at the two holes is that velocities between 0.5–1.3 km within the basement are higher at Hole 417D than at Hole 418A. Although the velocity profile at Hole 418A lies mostly within the 95% confidence interval of the Hole 417D velocity profile, the difference is probably significant because the rms error of fit is similar at the two holes (~0.020–0.035 s) and the differences in gradients are well supported by the confidence

Table 4. Data processing for circles. Numbers in parentheses are standard deviations.

Geophone depth (m)	Nominal range (km)	Number of shots	Average range (km)	Slowness at average range (s/km)	Average range after reduction to basement (km)
81	4	37	4.070 (0.134)	0.2039	2.162 (0.007)
	6	63	6.005 (0.133)	0.1852	4.289 (0.005)
230	2	77	2.022 (0.153)	0.1554	0.594 (0.001)
	4	144	4.009 (0.156)	0.2040	2.092 (0.006)
	6	65	5.995 (0.139)	0.1853	4.283 (0.021)
	8	71	8.010 (0.140)	0.1745	6.408 (0.019)
330	2	80	1.990 (0.141)	0.1541	0.574 (0.001)
	4	112	3.980 (0.168)	0.2020	2.083 (0.006)
	6	69	6.011 (0.163)	0.1877	4.273 (0.013)
	8	80	8.009 (0.135)	0.1786	6.365 (0.019)
430	2	75	2.004 (0.122)	0.1422	0.704 (0.001)
	4	141	4.004 (0.123)	0.1974	2.155 (0.006)
	6	67	6.010 (0.129)	0.1893	4.256 (0.014)
	8	83	7.995 (0.126)	0.1456	6.671 (0.015)

limits. Because velocity in the upper crust, which is measured on a scale of seismic wavelength, is thought to be controlled by crack porosity (Anderson et al., 1982; Stephen and Harding, 1983), the difference between Holes 418A and 417D may be due to more extensive fracturing of massive basalt flows and dikes at Hole 418A or to more extensive sealing of fractures away from the spreading axis at Hole 417D.

ANISOTROPY

Methodology

After the traveltimes from circle shot patterns had been reduced to basement, the times were fit by least squares with Fourier functions:

$$y = a_o + a_1\sin(\theta) + b_1\cos(\theta) + a_2\sin(2\theta) + b_2\cos(2\theta) + \ldots \\ \ldots + a_6\sin(6\theta) + b_6\cos(6\theta),$$

where y is traveltime, θ is azimuth of the shot from the hole, and a_i and b_i are Fourier coefficients determined by regression. Only data shot on circles were used; data on intersecting radial lines were excluded. Phase and amplitude calculated from the coefficients are given in Table 9. Apparent velocity was calculated from the average range and traveltime for each circle, assuming rays traveled a straight, horizontal line through homogeneous crust from the ray entry point to the receiver. In Figures 19–22, the data are plotted with the sum of the 2θ and the $2\theta + 4\theta$ components.

Ray diagrams calculated using the velocity-depth function from the τ-ζ inversion were used to estimate the depth of penetration of energy from each circle (Fig. 23). In general, energy from circles shot at radii of 2 and 4 km pass through only the crust above the seismometers. Energy from circles shot at 6 and 8 km dive beneath the seismometers and sample crust down to ~1.6 km. Note that at each circle radius, with the exception of the 2-km circles, the average traveltime tends to increase as the depth of the seismometer decreases (Table 9). This reflects the slightly shallower depths and, therefore, slower velocities at which rays turn.

If our corrected T-X data still contained significant systematic error due to the offset of the drillship from the hole, we would expect large amplitudes in the 1θ variations (period of 360°) among circles shot at any one seismometer depth. With one exception, the seismometer at 81 m, this is not the case. For the 4-km circle, the high 1θ amplitude is due to the data gap between 175° and 250°. For the 6-km circle, the variation may be due to offset of the drillship from the hole that was not corrected for by the average offset applied to the shot navigation. Significant 1θ variation occurs in all 4-km circles. It is unlikely, however, that errors in navigation can account for these variations because other circles without significantly high 1θ amplitudes were shot in between these circles. We conclude that navigation errors are negligible with the possible exception of the 6-km circle with receiver at 81 m.

Results

8-km Circles

Circles were shot at 8-km radii with the seismometer at 230, 330, and 430 m depth. The rays entered basement at a range of ~6.5 km and turned at a depth of ~1.5–1.6 km (Fig. 23). The large discrepancy between apparent velocity (5.2 km/s) and velocity at the ray turning point from the inversion model (6.8–6.9 km/s) is due to significant departure of the ray paths from a straight line.

The Fourier component that consistently has the highest amplitude is 3θ with a phase consistently toward the west (250°–300°). In the plots (Fig. 22), traveltimes appear almost randomly distributed with azimuth suggesting little significance to either the 3θ or the 2θ and $2\theta + 4\theta$ variations predicted by crustal models. At seismometer depths of 330 and 430 m, a significant decrease in traveltime (0.080–0.100 s) occurs between 260° and 300°. This feature also occurs at circles with radii of 4 km and is discussed subsequently.

6-km Circles

Circles were shot at 6-km radii with the seismometer at 81, 230, 330, and 430 m depth. Rays entered basement at a range of ~4.3 km and turned at depths of ~0.6–0.9 km (Fig. 23). The discrepancy between apparent velocity (~4.9 km/s) and inversion velocity at the turning depth (5.3–5.9 km/s) is less than that for the 8-km circles because the curvature of the ray paths is less.

For 6-km circles, no single component has the largest relative amplitude at all seismometer depths. At three out of four (430, 330, and 81 m), 1θ variation has the largest amplitude (Table 9). In these three circles, early arrivals consistently occur from the west to northwest (250°–360°). This feature also occurs at the fourth seismometer depth (230 m; Fig. 21), but the anomaly is apparently too narrow to produce a significant 1θ signal.

Traveltime variations with periods of 180° at 330 and 81 m depth have large relative amplitudes (Table 9) and appear in azimuth plots (Fig. 21). The amplitude of the 4θ variation at 430 m depth and the 3θ variation at 230 m are relatively large, but variations at such periods are not obvious in azimuth plots.

4-km Circles

Circles were shot at 4-km radii with the seismometer at 81, 230, 330, and 430 m depth. All amplitudes for the 81-m seismometer depth are unreliable because a large data gap influenced the Fourier decomposition (Fig. 20). Rays entered basement at a range of ~2.1 km and reached the receiver traveling downward only a few degrees above horizontal (Fig. 23). The

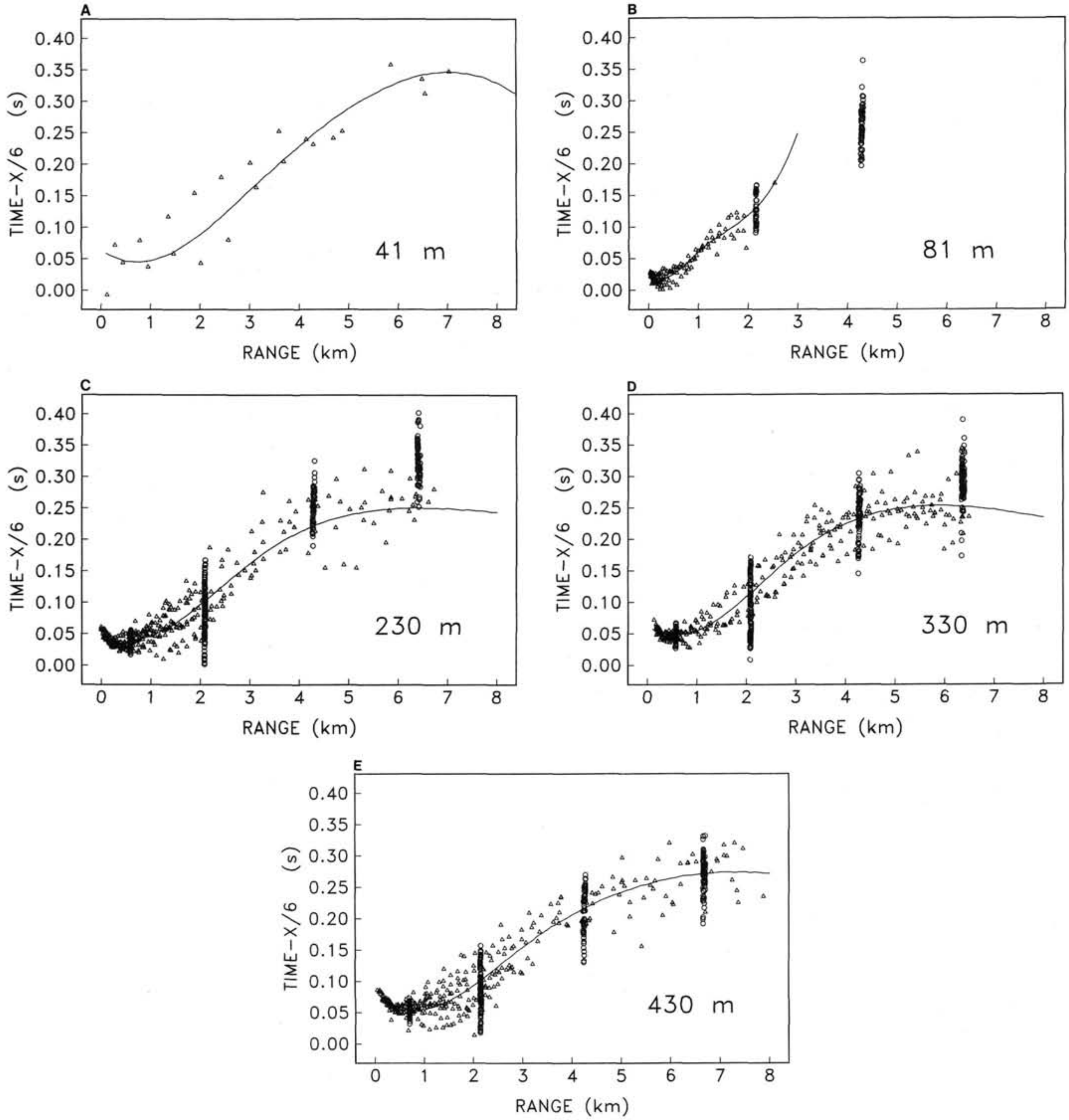

Figure 10. T-X plot of *P*-wave first arrivals after reduction to basement using interpolated water depth and constant sediment thickness. Time reduced at 6 km/s. Triangles indicate shots on radial lines; circles indicate shots on circles. Line is best cubic-spline fit to radial data only. Seismometer at (A) 41, (B) 81, (C) 230, (D) 330, and (E) 430 m.

apparent velocity (~5.2 km/s) exceeds the inversion model velocities (~5 km/s) only slightly.

Large-amplitude 1θ variations occur in traveltime at all 4-km circles, with the latest arrivals (slowest inferred velocity) from the south. In data from the three deeper receiver locations, a significant traveltime anomaly (hereafter, the "290° anomaly") of 0.080–0.100 s occurs between 250° and 300°. The feature has azimuth and amplitude similar to anomalies previously described in data shot at the 8-km range; however, the angle subtended by the anomaly at 4 km is broader. The 2θ variations have large amplitudes. However, these variations are not significant because the earliest arrivals in the 290° anomaly occur 90°–100° clockwise of the late arrival peak in the 1θ variation (Fig. 20).

2-km Circles

Circles were shot at 2-km range to seismometers at 230, 330, and 430 m depth. Rays from these circles enter basement at ranges of ~0.6 km and pass obliquely to the receiver. Apparent

Table 5. Segments of radial line data used in τ-ζ inversion.

Geophone depth (m)	Number of shots	Ray direction[a]	Mean slowness (s/km)	Mean τ (s)	Mean ζ (s)	ζ rms error (s)	τ rms error (s)
41	24	Up	0.19840	1.22197	0.00662	2.61293	0.04960
230	60	Up	0.17925	1.63182	0.10594	0.20412	0.03610
	179	Down	0.15292	0.23628	0.03140	0.05261	0.01880
	59	Down	0.20642	0.73679	−0.02796	0.11085	0.01880
330	113	Up	0.18722	1.46193	0.07200	0.14878	0.02900
	29	Up	0.14602	1.99476	0.25159	0.14430	0.02900
	113	Down	0.14662	0.23167	0.04413	0.04271	0.01280
	29	Down	0.20903	0.72171	−0.02138	0.09567	0.01280
430	85	Up	0.18311	1.68962	0.07638	0.20258	0.02940
	3	Up	0.14825	2.39790	0.24610	0.17443	0.02940
	146	Down	0.13776	0.28263	0.05676	0.04772	0.02070
	69	Down	0.20070	0.79905	−0.01860	0.11221	0.02070

[a] Direction of rays at geophone relative to horizontal plane.

Table 6. Results of τ-ζ inversion. Minimum and maximum depths are 95% confidence intervals.

Velocity (km/s)	Depth (km)	Minimum depth (km)	Maximum depth (km)
4.545	0.0		
5.342	0.637	0.546	0.729
5.580	0.770	0.687	0.854
6.849	1.511	1.397	1.624

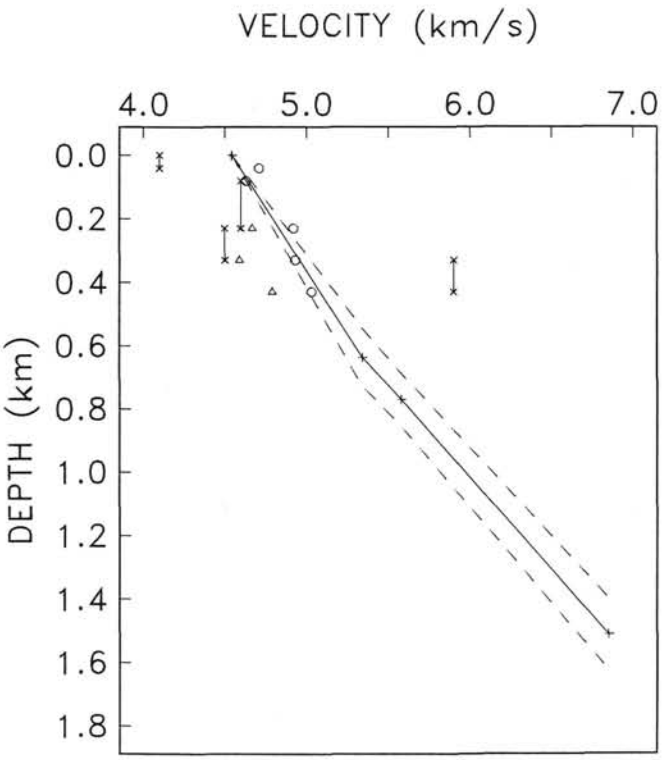

Figure 11. Velocity profile from τ-ζ inversion of data using interpolated water depth and constant sediment thickness (Table 6). Solid line connecting crosses indicates best depths determined by inversion. Dashed lines are 95% confidence limits on depths. Inflection point velocities are from Table 3: circles, before reduction to basement; triangles, after reduction to basement. Vertical lines connecting stars are interval velocities from Table 8. Interval velocity between 41 and 81 m (2.4 km/s) is off scale to left.

velocities for these circles (~4.4 km/s) agree with the surface velocity assumed in the inversion model (4.54 km/s).

The 2θ component of all 2-km circles has high relative amplitude (Table 9). The azimuth plots indicate that addition of the 4θ component adds little to the quality of fit (Fig. 19). The traveltime anomaly can be interpreted as P-wave velocity anisotropy with an amplitude of ± 0.22 km/s (~5%). Late traveltimes (slow velocities) arrive from the north and south. The phase rotates counterclockwise from 8° to 322° with increasing seismometer depth (Fig. 24). The average phase (346°) is ~54° oblique to the paleospreading direction (~292°; Rabinowitz et al., 1980).

DISCUSSION

Buried Seamounts

The traveltime anomaly centered at 290° is probably due to a buried basement peak or seamount. Navigation error cannot be responsible. Using the variation in traveltime with range observed on radial lines (Fig. 8), the magnitude of the anomaly (0.08–0.10 s) requires a systematic range error of 1.5–2 km that is much larger than potential navigation errors. Simple traveltime calculations show that the observed traveltime anomaly (~0.09 s) could be produced by a seamount, assuming a velocity of 4.5 km/s, with 0.27-km relief buried beneath sediment with a velocity of 1.8 km/s. For a seamount with a height equal to the assumed sediment thickness (0.324 km), a lower seamount velocity of 3.6 km/s would be required to produce the observed traveltime anomaly. Although mineral alteration associated with long-term exposure of basalt to seawater reduces seismic velocity, alteration at Hole 417A reduced velocities by only ~0.5 km/s below the average at Hole 417D (Salisbury et al., 1980b). So if the seamount exists, it is likely buried.

In reflection profiles, such a seamount would have relief of ~0.3 s two-way traveltime. A seamount does not appear in the depth-to-basement map of Senske and Stephen (this volume). However, the profiles may have been interpreted incorrectly. Figure 25 shows three profiles that cross near the ray entry points of the anomaly. Although there is no obvious basement high and no significant hyperbolae within shallow portions of the sediment section at ranges of ~2 km, there is a region where sediment returns show unusual lack of coherence. This absence of reflectors may indicate anomalous structure. Embley et al.'s (1983) interpretation of basement peaks in the eastern Nares Abyssal Plain on the basis of heat flow shows a similar absence of reflectors in surface-ship 3.5-kHz profiles. Elsewhere in the Nares Abyssal Plain, faulting in 3.5-kHz records is often an indication of a basement peak that cannot be resolved in air gun reflection profiles (Tucholke et al., 1986). The top of these base-

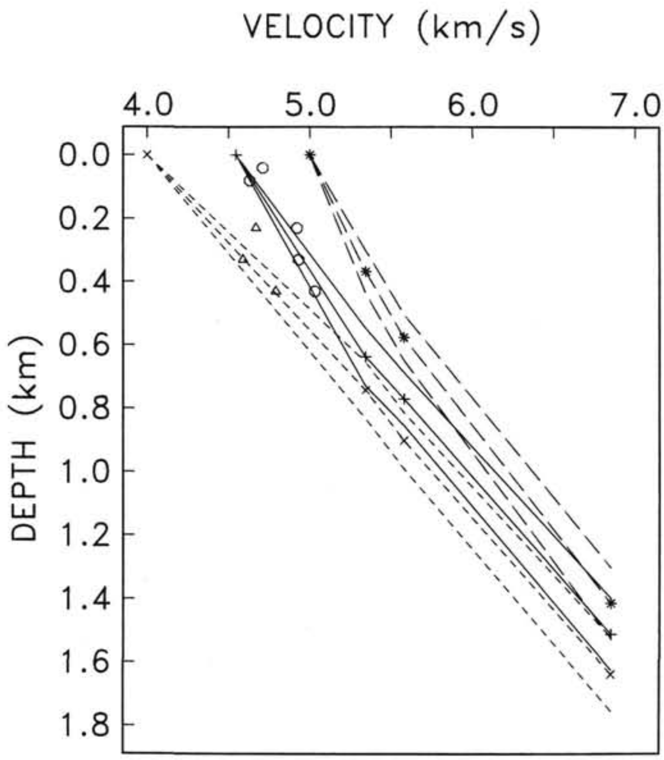

Figure 12. Velocity profiles from inversions assuming different velocities at top of basement. Solid lines connecting crosses are from Figure 11 (Table 6) with V_{surf} = 4.545 km/s. Dashed lines connecting crosses and stars indicate results assuming, respectively, V_{surf} = 4.0 km/s and V_{surf} = 5.0 km/s. Inflection point velocities (Table 3) agree best with inversion using a surface velocity near 4.5 km/s.

ment structures may be too narrow and their sides too steep to return coherent side echoes.

If the anomaly were due to crustal velocity variation in the upper 500 m, a relatively small, high velocity block would have to be present. Distributing the traveltime anomaly evenly between the ray entry points of the 4- and 2-km circles (~1.5 km), the apparent velocity increase would be 2.5 (230-m seismometer) to 3.7 km/s (430-m seismometer), or 50%–70%. These velocities (7.8–9.0 km/s) indicate upper mantle rock. The absence of a consistent traveltime anomaly at similar azimuths from shots in the 6-km circle indicates that the hypothetical high-velocity block would have to be detached from the underlying mantle.

A similar traveltime anomaly occurs at similar azimuths in data from 8-km circles at 2 of 3 seismometer depths: 330 and 430 m (Fig. 22). These ray paths probably pass through another seamount (Fig. 25) located 4 km away along a tectonic flow line (the azimuth, 290°, is nearly parallel to the paleospreading direction).

Table 7. Velocities and densities used in calculating full-waveform reflectivity seismograms. Depths indicate base of intervals. Last column gives the number of layers into which each interval was divided in order to perform calculations.

Depth (km)	Composition	*P*-wave velocity (km/s)	*S*-wave velocity (km/s)	Density (g/cm^3)	Number of layers
5.511	Water	1.516	0.8753	1.0300	1
5.521	Sediment	1.800	0.5000	0.9338	1
5.835	Sediment	1.800	0.5000	0.9338	1
5.840	Basement	4.545	2.4998	1.9736	1
6.472	Basement	5.342	2.9381	2.2755	25
6.605	Basement	5.580	3.0690	2.3657	6
7.346	Basement	6.849	3.7670	2.8464	14

Anisotropy in the Shallow Crust (0–0.5 km)

The OSE at Hole 418A resolves velocity variations horizontally to ~0.5 km. Anisotropy corresponding to 2θ variation in the arrivals from shots at 2 km (~0.6-km radius on basement) is ±0.22 km/s or ±5%. At Hole 504B, Little and Stephen (1985) used similar methods and found amplitudes twice our value. If velocity variation is due to seawater-filled cracks (Little and Stephen, 1985; Stephen, 1985; Shearer and Orcutt, 1985), the smaller magnitude may be due to infilling of voids by diagenetic minerals. At Hole 504B, slow velocities were oriented in the spreading direction, whereas at Hole 418A the phases are 24°–68° oblique to the paleospreading direction. Elsewhere, we

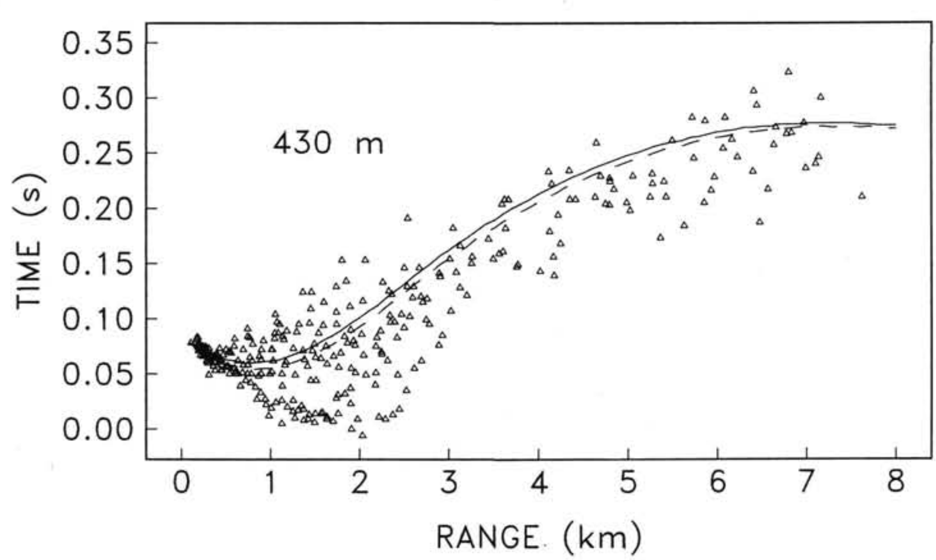

Figure 13. Traveltimes calculated by ray tracing through the τ-ζ velocity model in Figure 11. Time reduced at 6.8 km/s. Solid line shows traveltime curve calculated for model velocities. Data (triangles) and best cubic-spline fit (dashed line) are from Figure 10E.

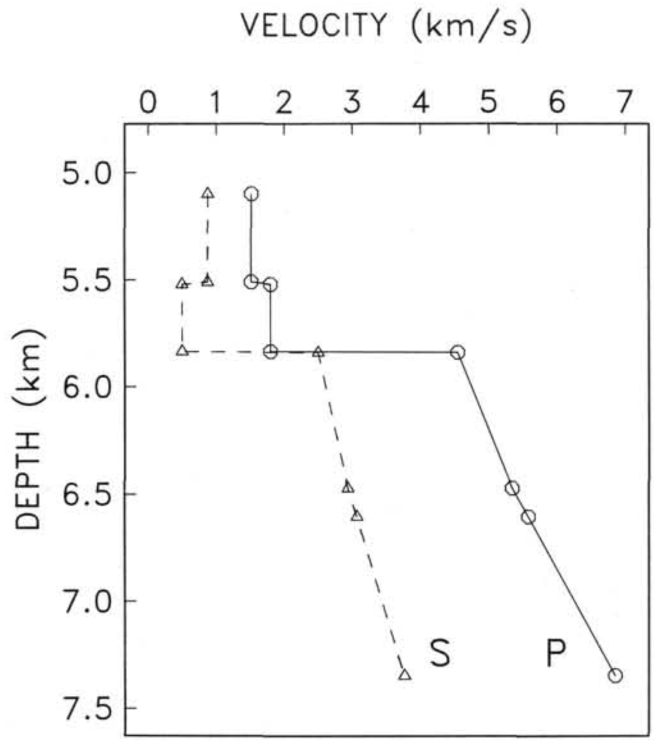

Figure 14. *P*- and *S*-wave velocities (from Table 7) used to calculate reflectivity seismograms. Constant water velocities above 5.1 km are not shown.

suggest that the cracks and voids that affect seismic velocity in the shallowest crust are related to extrusive processes rather than (or in addition to) tectonic stress (S. A. Swift and R. A. Stephen, unpubl. data). Velocity anisotropy unrelated to spreading direction may be produced by small volcanoes (0.2–0.3 km high) that are common at slow-spreading centers like the Mid-Atlantic Ridge (Ballard and van Andel, 1977) but uncommon at fast-spreading centers (Ballard et al., 1979).

Anisotropy in the Mid-Crust Region (0.5–1.5 km)

The mid-crust region was sampled by circle shooting at ranges of 6 and 8 km. Velocities indicate that this depth region corresponds with seismic Layers 2B and 2C. The geology of these layers has been interpreted as sheeted dikes and transition zones to pillow basalts above and gabbros below (e.g., Anderson et al., 1982; Shearer and Orcutt, 1985).

No significant traveltime variation with either 2θ or $2\theta + 4\theta$ periods was found in 6- and 8-km circles at Hole 418A. Elsewhere, anisotropy has been reported in arrivals passing through these layers. Shearer and Orcutt (1985) found significant 2θ variation in data from 140 Ma crust in the South Pacific. *P*-waves arrived early from azimuths at 90° to early arrivals from the upper mantle, and thus were inferred to have traveled parallel to the former ridge crest. Shearer and Orcutt (1985) attributed anisotropy to velocity reduction by saturated cracks oriented parallel to the ridge crest. In a study of 1-3-Ma crust in the North Atlantic, White and Whitmarsh (1984) describe a 4θ variation in *P*-wave arrival times oriented oblique to the trend of magnetic anomalies. They also attribute anisotropy to saturated cracks.

The absence of significant 2θ or 4θ traveltime variation from crust >0.5 km depth at Hole 418A appears unrelated to age, even though the number of studies (3) is small. We suggest that the mid-crustal voids or cracks interpreted elsewhere do not occur at Hole 418A either because they did not originally penetrate deep enough during ridge crest faulting or because such cracks were sealed off-ridge either by compression during plate realignment or by diagenetic mineralization. Deeper crustal drilling may be able to distinguish between these hypotheses.

CONCLUSIONS

P-wave velocity at Hole 418A increases with depth at a gradient of $\sim 1.5\ s^{-1}$ from 4.5 km/s at top of basement to 6.8 km/s at 1.5 km depth. The velocity profile at Hole 418A differs from that at Hole 417D. Between 0.5–1.2 km, the velocities at Hole 418A are ~0.25 km/s lower than at Hole 417D. Higher velocities at Hole 417D may be due to lower porosities caused by less initial fracturing at the spreading center or to more complete sealing of fractures off axis.

Lithology below ~0.2 km at Hole 418A may not be representative of the local region. OSE velocities measured within a radius of 6 km are 0.25–0.5 km/s lower than sonic log velocities. Either the volcanic extrusive layer of relatively low-velocity pillow basalts is thicker elsewhere or closing of cracks on the same scale as the pillows is more prevalent at Hole 418A.

Horizontal anisotropy of *P*-wave velocities in the upper crust is ±0.22 km/s (~5%). The phase is oblique to the paleospreading direction and rotates counterclockwise with depth. Anisotropy was measured only within the extrusive layer (upper 0.5 km) and only within ±0.6 km of the hole. Velocities measured on rays turning between 0.5–1.5 km depth from ranges of 4–6 km did not show significant variations with 180° periods.

ACKNOWLEDGMENTS

We thank the ship officers and crew, drilling staff, and scientific and technical personnel of the *JOIDES Resolution* and the R/V *Fred H. Moore* for their assistance in carrying out the OSE. On the *Moore*, K. Griffith, A. Roberts, and their team of mechanical and electrical technicians carried out very effective air gun and water gun operations. The water gun was borrowed from the USGS-Woods Hole. J. Broda, G. Glass, and A. Roberts carried out explosives shooting on the *Moore*. Captain B. Collins and his officers navigated *Moore* shooting patterns extremely well, often to a resolution of less than 10 m.

We thank Captain E. Oonk on the *JOIDES Resolution* for use of the bridge radar and B. Hamlin and the ODP technicians for standing navigation watches. M. Reitmeyer and P. Thompson were effective in preparing tool and logging heads. We thank co-chief scientists M. Salisbury and J. Scott and ODP operations superintendent G. Foss for their support and co-operation.

M. Weiderspahn and W. Robinson (University of Texas) designed and wrote the digital acquisition system. W. Witzell maintained the borehole seismometer. D. Koelsch calibrated the radio shot-logging system. F. Hess designed and supervised construction of the three-component borehole preamplifier.

L. Gove and T. Bolmer wrote the software used in reducing the seismograms. Tom Bolmer assisted greatly in data processing. S. Little, L. Gove, and H. Hoskins helped solve numerous problems in our data analysis.

Funding provided from National Science Foundation Grant No. OCE-8416633. Woods Hole Oceanographic Institution contribution number 6388.

REFERENCES

Anderson, R. N., et al., 1982. DSDP Hole 504B, the first reference section over 1 km through Layer 2 of the oceanic crust. *Nature*, 300: 589–594.

Auroux, C. A., and Stephen, R. A., 1986. Geophysical profiling, ODP Leg 102. *In* Salisbury, M. H., Scott, J. H., et al., *Proc. ODP, Init. Repts.*, 102: College Station, TX (Ocean Drilling Program), 7–91.

Ballard, R. D., Holcomb, R. T., and van Andel, T. H., 1979. The Galapogos Rift at 86°W: 3. Sheet flows, collapse pits, and lava lakes of the rift valley. *J. Geophys. Res.*, 84:5407–5422.

Ballard, R. D., and van Andel, T. H., 1977. Morphology and tectonics of the inner rift valley at latitude 36°50′N on the Mid-Atlantic Ridge. *Geol. Soc. Am. Bull.*, 88:507–530.

Birch, F., 1961. The velocity of compressional waves in rocks to 10 kilobars, Part 2. *J. Geophys. Res.*, 66:2199–2224.

Bratt, S. R., and Purdy, G. M., 1984. Structure and variability of oceanic crust on the flanks of the East Pacific Rise between 11° and 13° N. *J. Geophys. Res.*, 89:6111–6125.

Christensen, N. I., Blair, S. C., Wilkens, R. H., and Salisbury, M. H., 1980. Compressional wave velocities, densities, and porosities of basalts from Holes 417A, 417D, and 418A, Deep Sea Drilling Project Legs 51 through 53. *In* Donnelly, T., Francheteau, J., Bryan, W., Robinson, P., Flower, M., Salisbury, M., et al., *Init. Repts. DSDP*, 51, 52, 53, Pt. 2: Washington (U.S. Govt. Printing Office), 1467–1471.

Christensen, N. I., and Salisbury, M. H., 1975. Structure and constitution of the lower oceanic crust. *Rev. Geophys. Space Phys.*, 13:57–86.

Donnelly, T., Francheteau, J., Bryan, W., Robinson, P., Flower, M., Salisbury, M., et al., 1980. *Init. Repts. DSDP*, 51, 52, 53: Washington (U.S. Govt. Printing Office).

Donnelly, T. W., Thompson, G., and Salisbury, M. H., 1980. The chemistry of altered basalts at Site 417, Deep Sea Drilling Project Leg 51. *In* Donnelly, T., Francheteau, J., Bryan, W., Robinson, P., Flower, M., Salisbury, M., et al., *Init. Repts. DSDP*, 51, 52, 53, Pt. 2: Washington (U.S. Govt. Printing Office), 1319–1330.

Dorman, L. M., and Jacobson, R. S., 1981. Linear inversion of body wave data. Part I. Velocity structure from traveltimes and ranges. *Geophysics*, 46:138–151.

Embley, R. W., Hobart, M. A., Anderson, R. N., and Abbott, D., 1983. Anomalous heat flow in the northwest Atlantic: a case for continued hydrothermal circulation in 80-MY crust. *J. Geophys. Res.*, 88: 1067–1074.

Fuchs, K., and Müller, G., 1971. Computation of synthetic seismograms with the reflectivity method and comparison with observations. *Geophys. J. R. Astron. Soc.*, 23:417–433.

Gutenberg, B., 1953. Wave velocities at depths 50–600 kilometers. *Bull. Seismol. Soc. Am.*, 43:223–232.

Kennett, B.L.N., and Orcutt, J. A., 1976. A comparison of travel time inversions for marine refraction profiles. *J. Geophys. Res.*, 81:4061–4070.

Little, S. A., and Stephen, R. A., 1985. Costa Rica rift borehole seismic experiment, DSDP Hole 504B, Leg 92. *In* Anderson, R. N., Honnorez, J., Becker, K., et al., *Init. Repts. DSDP*, 83: Washington (U.S. Govt. Printing Office), 517–528.

Purdy, G. M., 1982. The correction for the travel time effects of seafloor topography in the interpretation of marine seismic data. *J. Geophys. Res.*, 87:8389–8396.

________, 1987. New observations of the shallow seismic structure of young oceanic crust. *J. Geophys. Res.*, 92:9351–9362.

Purdy, G. M., and Ewing, J. I., 1986. Seismic structure of the oceanic crust. *In* Vogt, P. R., and Tucholke, B. E. (Eds.), *The Geology of North America: The Western North Atlantic Region*: Geol. Soc. Am., DNAG Series, 313–330.

Rabinowitz, P. D., Hoskins, H., and Asquith, S. M., 1980. Geophysical site survey results near Deep Sea Drilling Project Sites 417 and 418 in the central Atlantic Ocean. *In* Donnelly, T., Francheteau, J., Bryan, W., Robertson, P., Flower, M., Salisbury, M., et al., *Init. Repts. DSDP*, 51, 52, 53, Pt. 2: Washington (U.S. Govt. Printing Office), 629–669.

Salisbury, M. H., Donnelly, T. W., and Francheteau, J., 1980a. Geophysical logging in Deep Sea Drilling Project Hole 417D. *In* Donnelly, T., Francheteau, J., Bryan, W., Robertson, P., Flower, M., Salisbury, M., et al., *Init. Repts. DSDP*, 51, 52, 53, Pt. 2: Washington (U.S. Govt. Printing Office), 705–713.

Salisbury, M. H., Stephen, R. A., Christensen, N. I., Francheteau, J., Hamano, Y., Hobart, M., and Johnson, D., 1980b. The physical state of the upper levels of Cretaceous oceanic crust from the results of logging, laboratory studies, and the oblique seismic experiment at Deep Sea Drilling Project Sites 417 and 418. *In* Donnelly, T., Francheteau, J., Bryan, W., Robertson, P., Flower, M., Salisbury, M., et al., *Init. Repts. DSDP*, 51, 52, 53, Pt. 2: Washington (U.S. Govt. Printing Office), 1579–1597.

Shearer, P., and Orcutt, J., 1985. Anisotropy in the oceanic lithosphere - theory and observations from the Ngendi seismic refraction experiment in the south-west Pacific. *Geophys. J. R. Astron. Soc.*, 80:493–526.

Shipboard Scientific Party, 1986. Site 418: Bermuda Rise. *In* Salisbury, M. H., Scott, J. H., et al., *Proc. ODP, Init. Repts.*, 102: College Station, TX (Ocean Drilling Program), 95–149.

Spudich, P., and Orcutt, J., 1980a. A new look at the seismic velocity structure of the oceanic crust. *Rev. Geophys. Space Phys.*, 18:627–645.

________, 1980b. Petrology and porosity of an oceanic crustal site: results from wave form modeling of seismic refraction data. *J. Geophys. Res.*, 85:1409–1433.

Stephen, R. A., 1977. Synthetic seismograms for the case of the receiver within the reflectivity zone. *Geophys. J. R. Astron. Soc.*, 51:169–181.

________, 1981. Seismic anisotropy observed in upper oceanic crust. *Geophys. Res. Lett.*, 8:865–868.

________, 1985. Seismic anisotropy in the upper oceanic crust. *J. Geophys. Res.*, 90:11383–11396.

Stephen, R. A., and Bolmer, S. T., 1985. The direct wave root in marine seismology. *Bull. Seismol. Soc. Am.*, 75:57–67.

Stephen, R. A., and Harding, A. J., 1983. Travel time analysis of borehole seismic data. *J. Geophys. Res.*, 88:8289–8298.

Stephen, R. A., Louden, K. E., and Mathews, D. H., 1979. The oblique seismic experiment on DSDP Leg 52. *In* Donnelly, T., Francheteau, J., Bryan, W., Robertson, P., Flower, M., Salisbury, M., et al., *Init. Repts. DSDP*, 51, 52, 53, Pt. 2: Washington (U.S. Govt. Printing Office), 675–704.

Tucholke, B. E., Shephard, L. E., and Swift, S. A., 1986. Site assessment studies for sub-seabed disposal of nuclear waste, 1986: Geologic framework of the Nares Abyssal Plain: Albuquerque, NM (Sandia National Laboratories).

White, R. S., and Stephen, R. A., 1980. Compressional to shear wave conversion in oceanic crust. *Geophys. J. R. Astron. Soc.*, 63:547–565.

White, R. S., and Whitmarsh, R. B., 1984. An investigation of seismic anisotropy due to cracks in the upper oceanic crust at 45°N, Mid-Atlantic Ridge. *Geophys. J. R. Astron. Soc.*, 79:439–467.

Date of initial receipt: 5 January 1987
Date of acceptance: 14 July 1987
Ms 102B-117

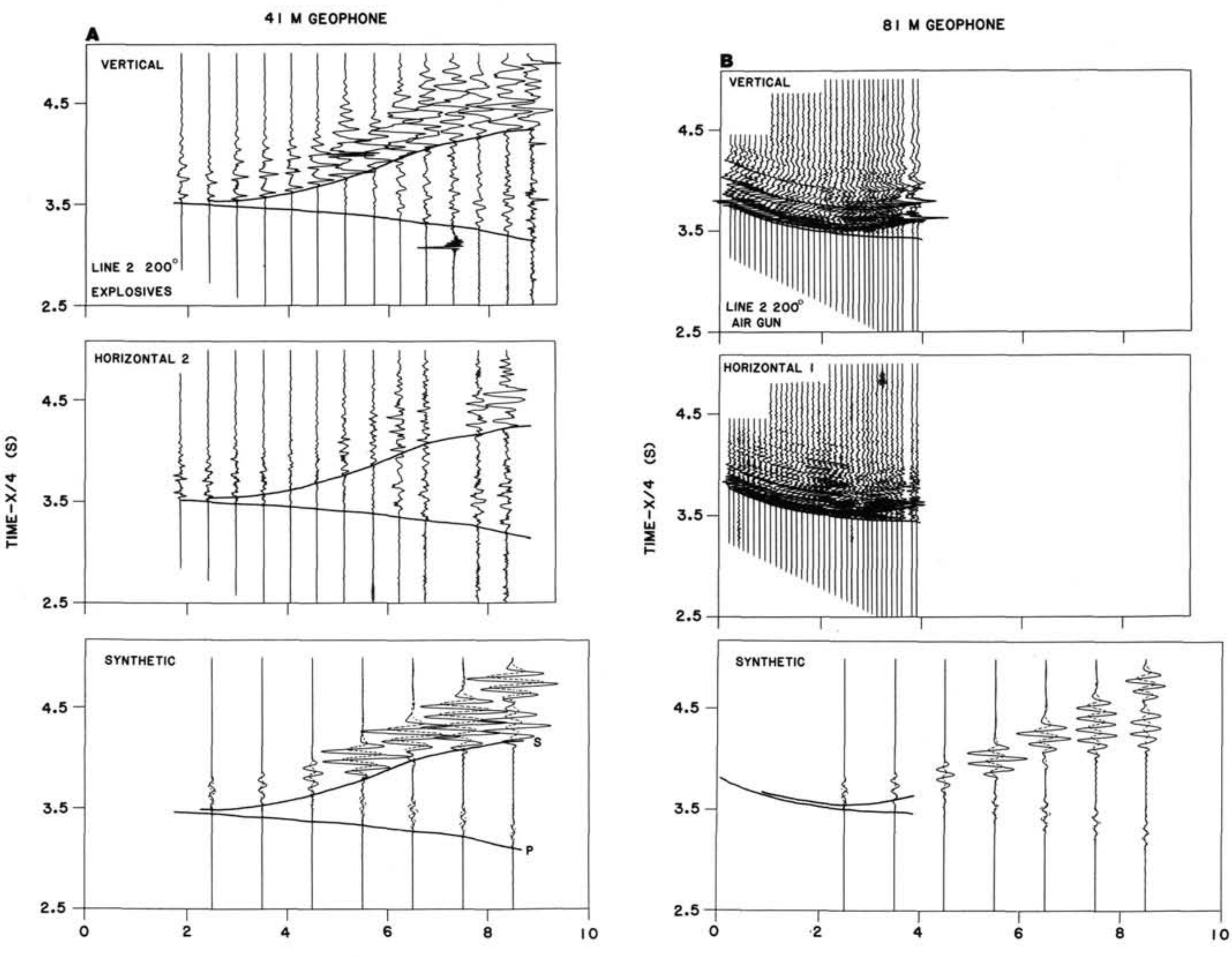

Figure 15. Comparison of reflectivity seismograms with data from each geophone depth. In synthetics, the vertical component is the solid line, and the horizontal component is dashed. Observed seismograms were bandpass filtered at 5–50 Hz and scaled by range as in Figure 6. Amplitude scaling of air gun records is 6 times that of explosives. A. 41-m explosives. B. 81-m air gun. C. 230-m explosives. D. 230-m air gun. E. 330-m air gun. F. 430-m explosives. G. 430-m air gun.

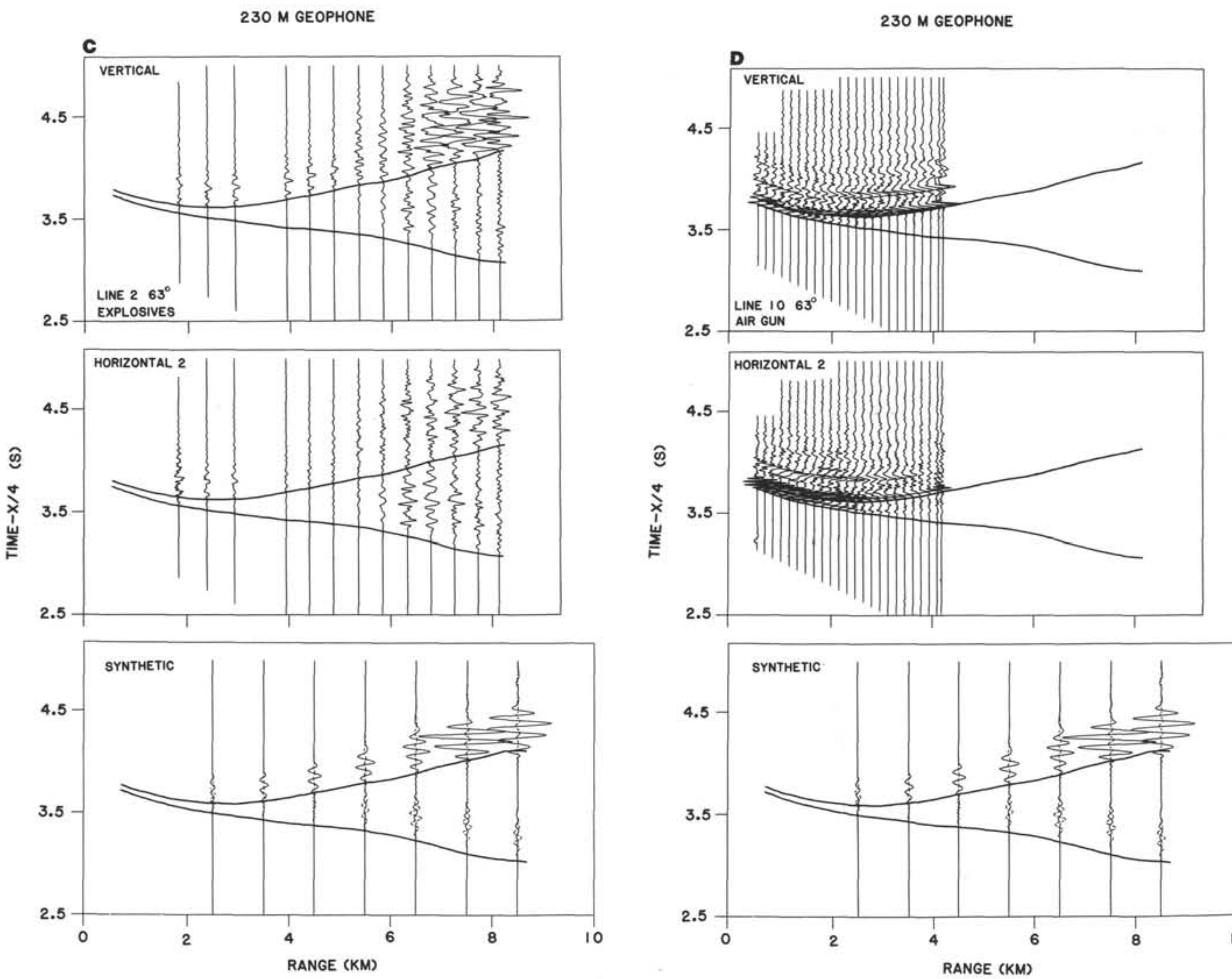

Figure 15. (continued).

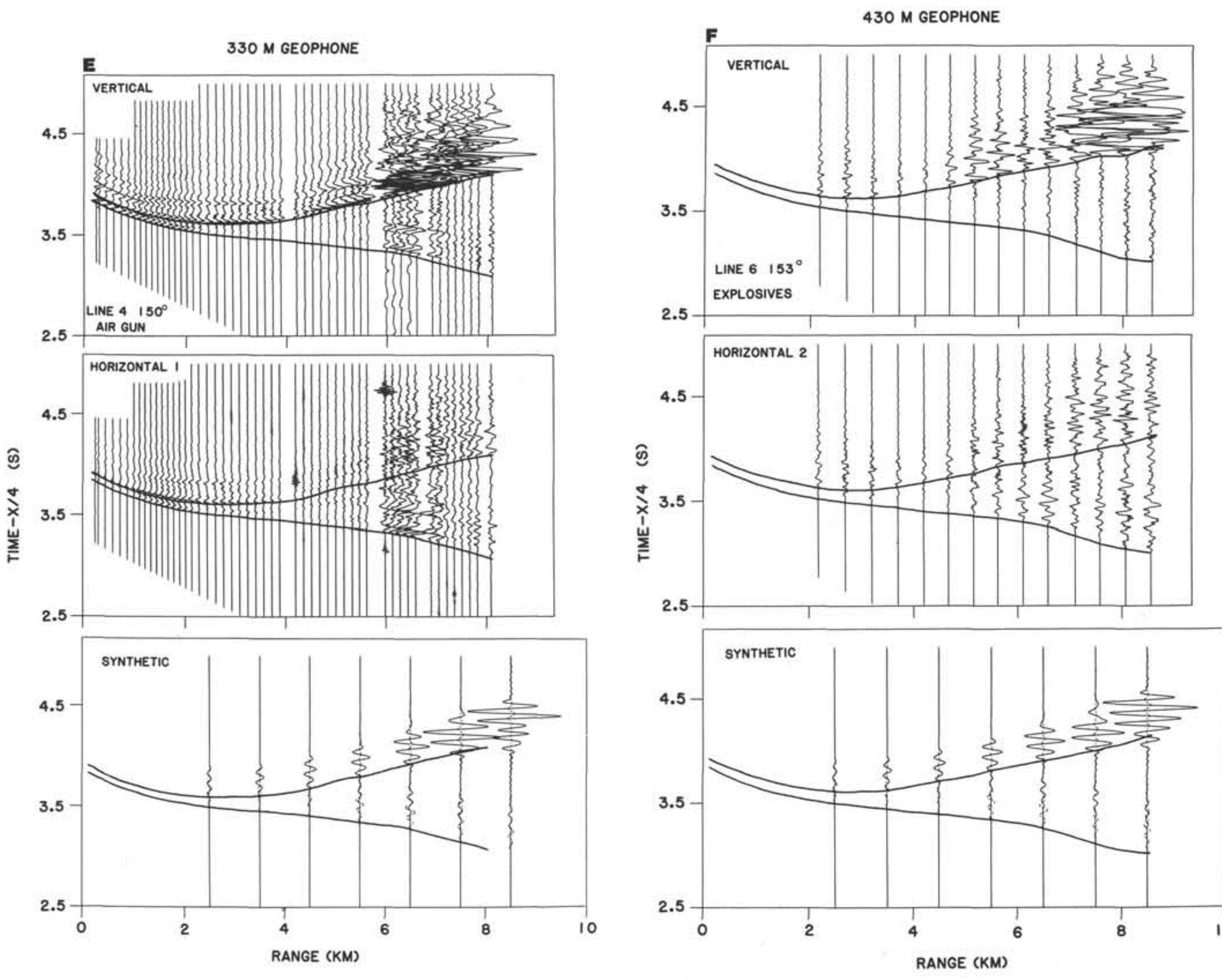

Figure 15. (continued).

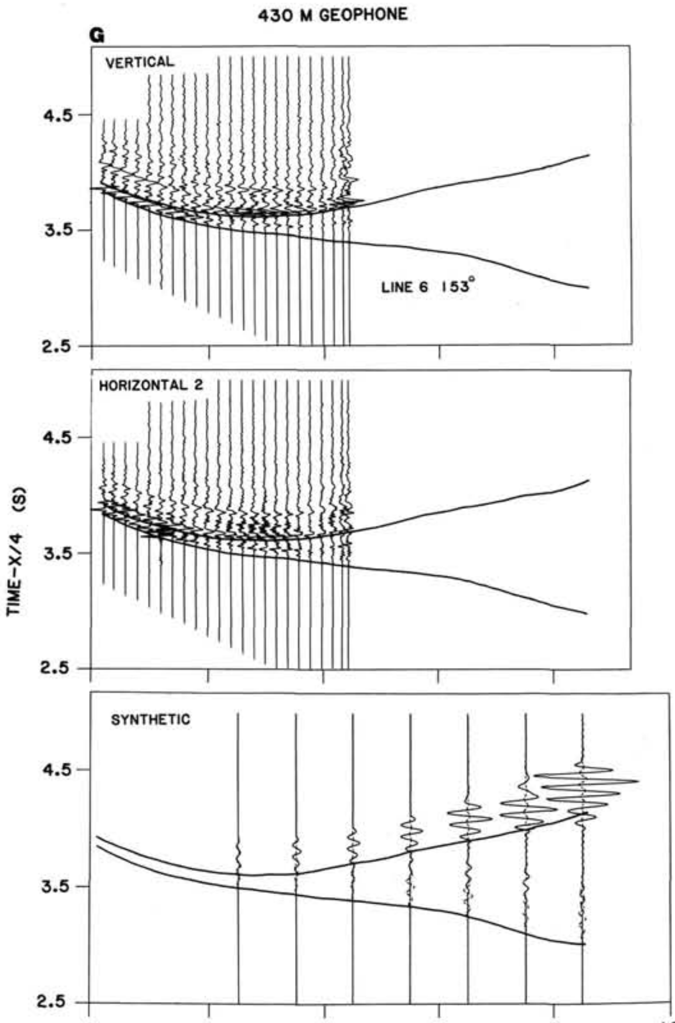

Figure 15. (continued).

Table 8. *P*-wave interval velocities from near-vertical incidence arrivals.

Depth interval (m within basement)	Velocity (km/s)
0–41	4.1
41–81	2.4
81–230	4.6
230–330	4.5
330–430	5.9

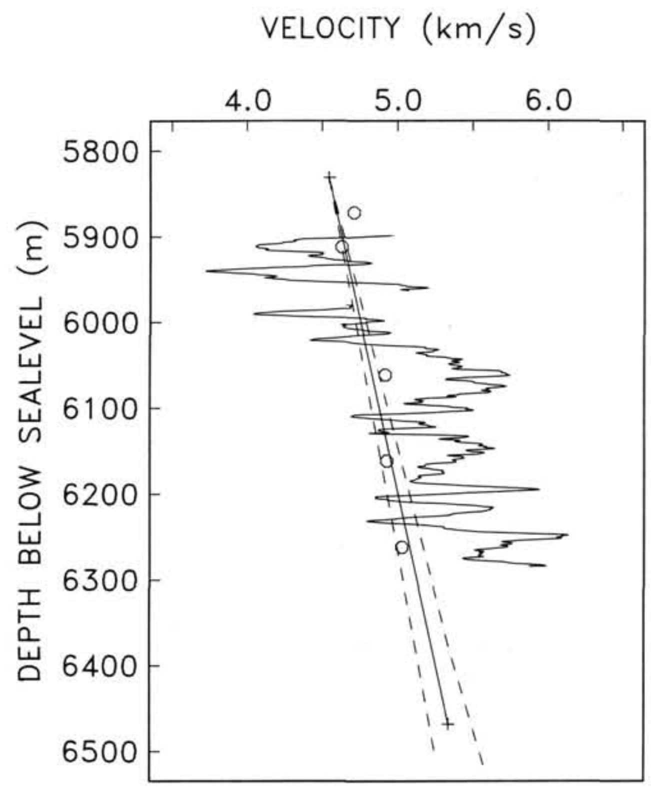

Figure 16. Comparison of velocities from τ-ζ inversion and inflection point method with velocities from the sonic tool. Sonic log is flat moving average of velocities over ~7 m.

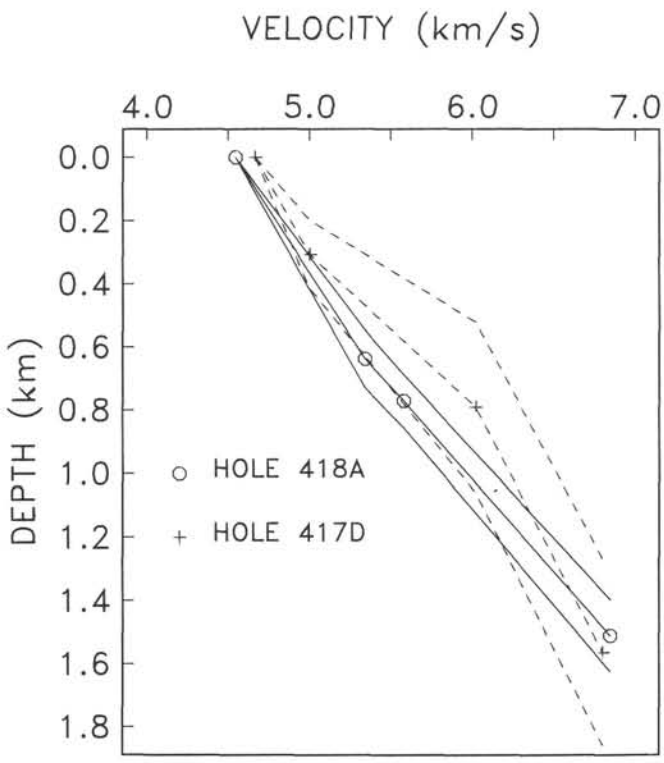

Figure 17. Comparison of τ-ζ inversion profile at Hole 418A (solid line) with that at Hole 417D (dashed line). For each profile, the middle trace indicates the best depths determined by the inversion; upper and lower traces are the 95% confidence limits.

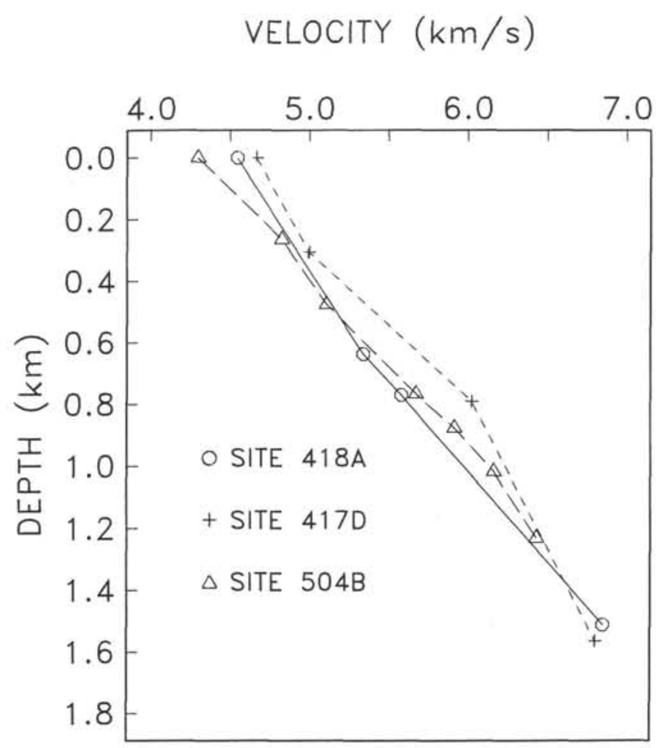

Figure 18. Comparison of inversion profile from Hole 418A with profiles at Hole 417D (110 Ma, western North Atlantic; Stephen and Harding, 1983) and at Hole 504B (6 Ma, Costa Rica Rift; Little and Stephen, 1985). See Figure 17 for key to traces.

Table 9. Fourier decomposition of *P*-wave traveltimes from circles. Numbers in parentheses are standard deviations.

Geophone depth (m)	Average range (km)		Mean traveltime (s)	Apparent velocity (km/s)	Theta	Phase	Amplitude (s)
	Shooting	Basement					
81	4.070	2.162	0.416	5.20			
	(0.134)	(0.007)			1	46	0.059
					2	259	0.055
					3	108	0.058
					4	338	0.026
					5	190	0.024
					6	21	0.010
81	6.006	4.289	0.892	4.81			
	(0.133)	(0.005)			1	128	0.025
					2	146	0.020
					3	46	0.013
					4	330	0.007
					5	271	0.004
					6	40	0.005
230	2.022	0.594	0.126	4.71			
	(0.153)	(0.001)			1	156	0.008
					2	8	0.006
					3	125	0.004
					4	133	0.006
					5	174	0.003
					6	96	0.001
230	4.009	2.092	0.398	5.26			
	(0.156)	(0.006)			1	145	0.041
					2	21	0.020
					3	223	0.010
					4	180	0.010
					5	130	0.012
					6	286	0.003
230	5.995	4.283	0.893	4.80			
	(0.139)	(0.021)			1	42	0.017
					2	273	0.012
					3	236	0.029
					4	224	0.021
					5	172	0.028
					6	136	0.027
230	8.010	6.408	1.268	5.05			
	(0.140)	(0.019)			1	289	0.013
					2	20	0.013
					3	248	0.022
					4	340	0.014
					5	239	0.015
					6	76	0.009
330	1.990	0.574	0.133	4.32			
	(0.141)	(0.001)			1	221	0.005
					2	349	0.009
					3	83	0.004
					4	106	0.003
					5	215	0.001
					6	153	0.0002
330	3.980	2.083	0.392	5.31			
	(0.168)	(0.006)			1	196	0.046
					2	59	0.026
					3	176	0.019
					4	297	0.015
					5	66	0.007
					6	169	0.001
330	6.011	4.273	0.862	4.96			
	(0.163)	(0.013)			1	138	0.034
					2	96	0.025
					3	42	0.008
					4	304	0.008
					5	161	0.013
					6	360	0.008
330	8.009	6.365	1.230	5.17			
	(0.135)	(0.019)			1	60	0.011
					2	70	0.011
					3	299	0.019
					4	258	0.014
					5	263	0.009
					6	64	0.015
430	2.004	0.704	0.162	4.34			
	(0.122)	(0.001)			1	242	0.005
					2	322	0.007
					3	113	0.004
					4	136	0.003
					5	154	0.002
					6	326	0.001

Table 9 (continued).

Geophone depth (m)	Average range (km) Shooting	Basement	Mean traveltime (s)	Apparent velocity (km/s)	Theta	Phase	Amplitude (s)
430	4.004	2.155	0.408	5.28			
	(0.123)	(0.006)			1	161	0.031
					2	17	0.018
					3	251	0.017
					4	198	0.009
					5	105	0.014
					6	348	0.004
430	6.010	4.256	0.839	5.07			
	(0.129)	(0.014)			1	78	0.036
					2	122	0.008
					3	126	0.013
					4	330	0.015
					5	173	0.013
					6	354	0.010
430	7.995	6.672	1.253	5.32			
	(0.126)	(0.015)			1	141	0.006
					2	80	0.003
					3	267	0.015
					4	228	0.015
					5	174	0.009
					6	68	0.009

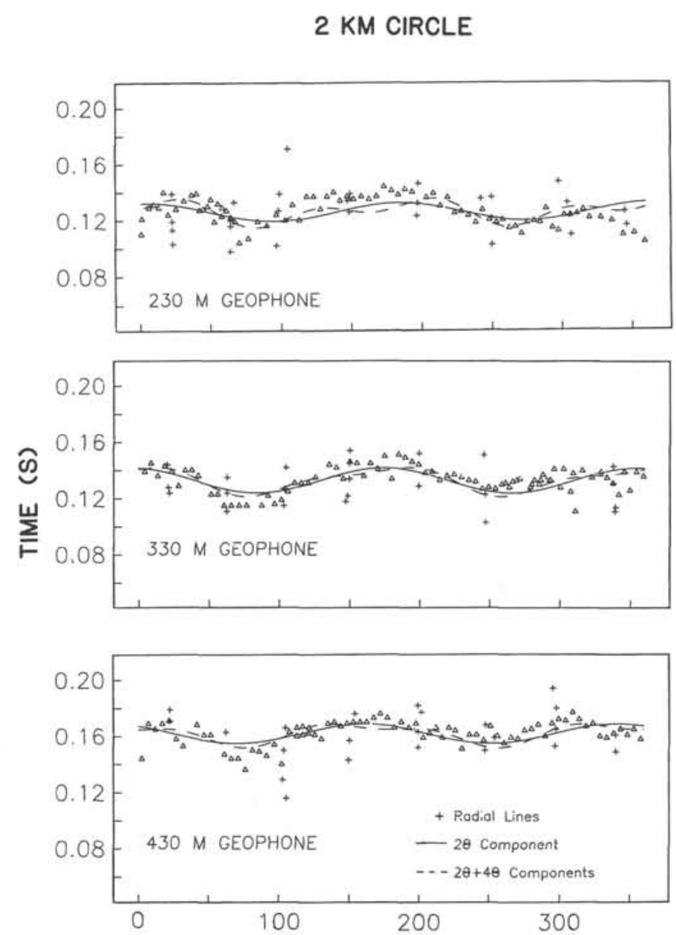

Figure 19. *P*-wave arrivals reduced to basement from shots on circular lines plotted against azimuth of shot from drill hole. Circles shot at a radius of 2 km. Triangles are data; crosses are arrivals from shots on radial lines within a range window of 0.2–0.3 km centered on the intersected circle. Solid line is the best-fit curve with only the mean and the 2θ components; dashed line includes 4θ component as well. Traveltimes have not been range reduced.

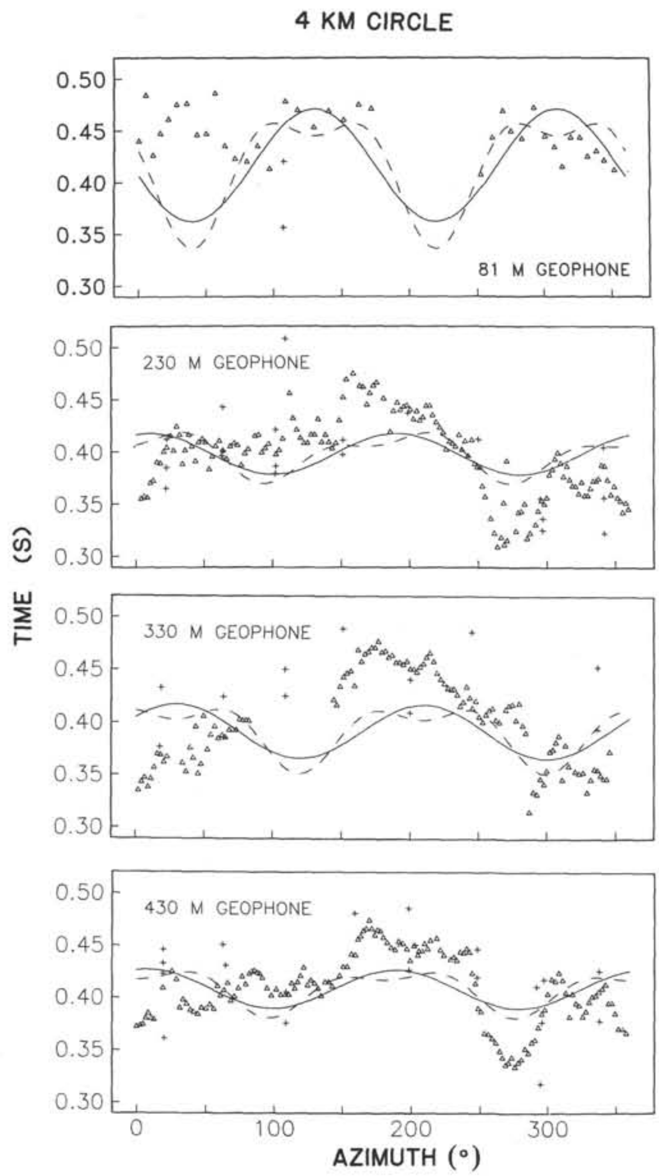

Figure 20. *P*-wave arrivals reduced to basement for shooting radius of 4 km. Symbols as in Figure 19. Range window for intersecting radial lines is 0.4 km.

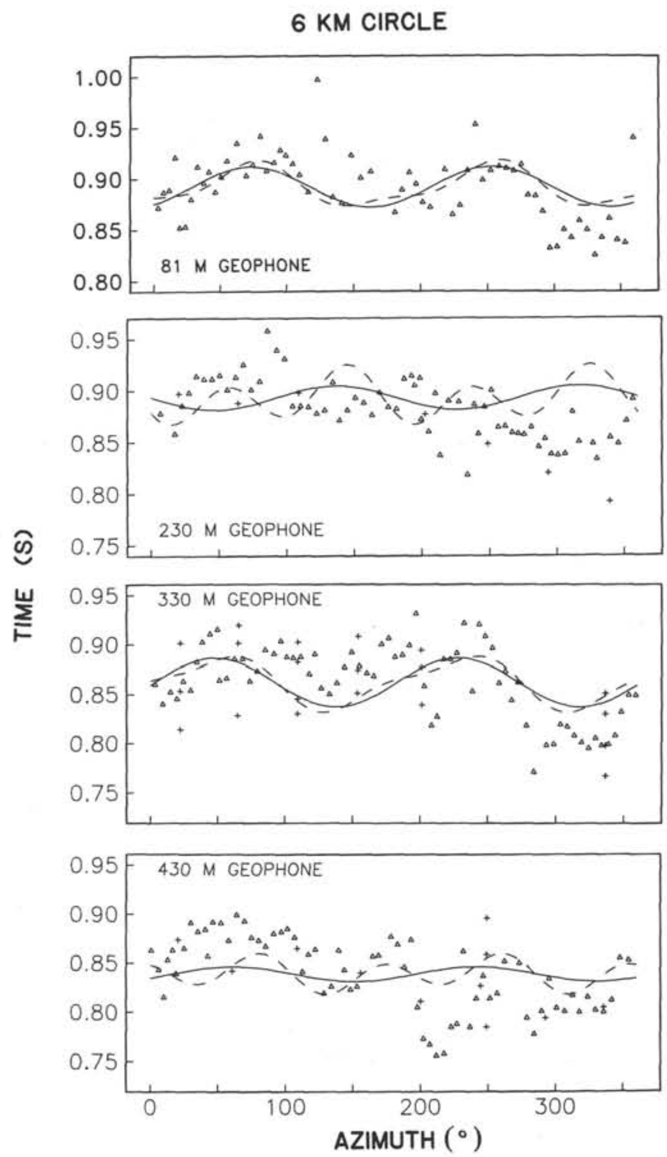

Figure 21. *P*-wave arrivals reduced to basement for shooting radius of 6 km. Symbols as in Figure 19. Range window for intersecting radial lines is 0.6 km.

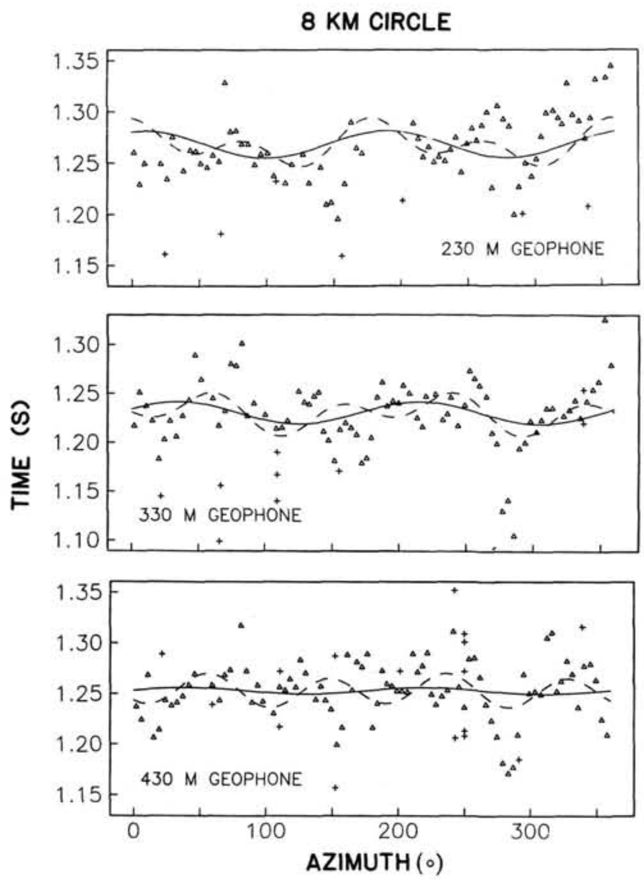

Figure 22. *P*-wave arrivals reduced to basement for shooting radius of 8 km. Symbols as in Figure 19. Range window for intersecting radial lines is 0.5 km.

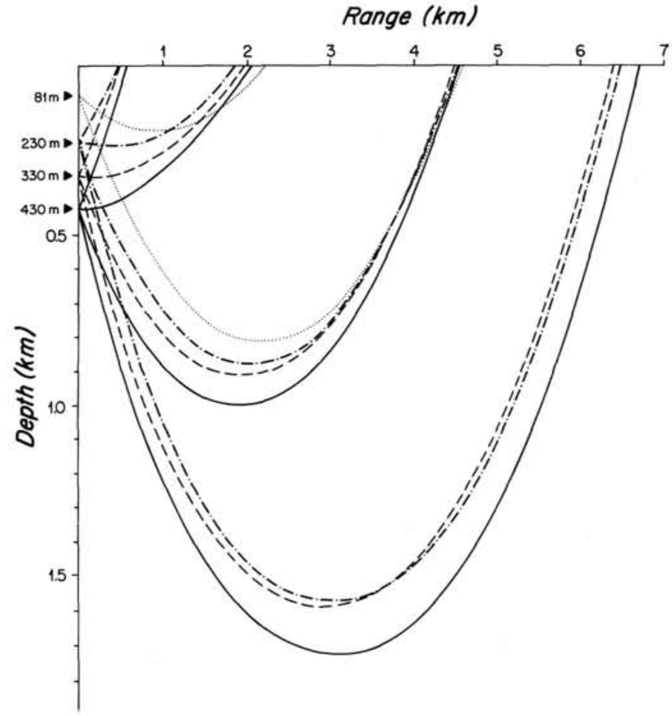

Figure 23. Rays traced through velocity model in Table 6 for circles with shooting radii of 2, 4, 6, and 8 km. Seismometer locations labeled with depth (m) below sediment/basement contact. Velocity model was modified by linearly extrapolating the gradient between 0.770 and 1.511 km to 2 km depth.

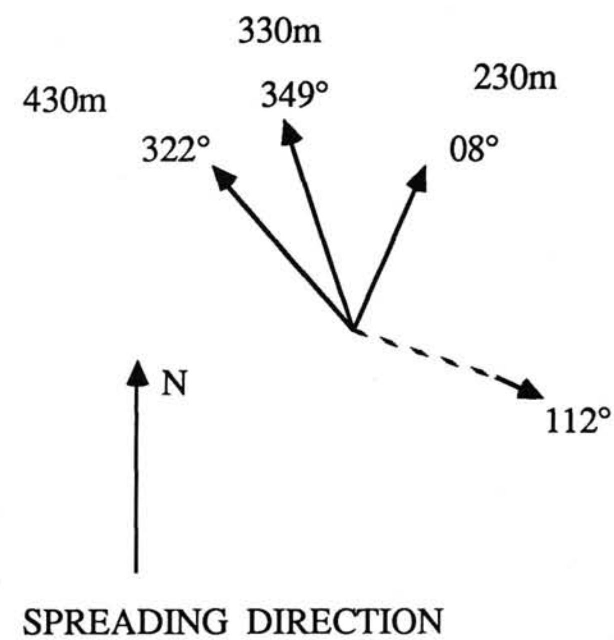

Figure 24. Rotation of the slow direction with seismometer depth in the 2-km circle.

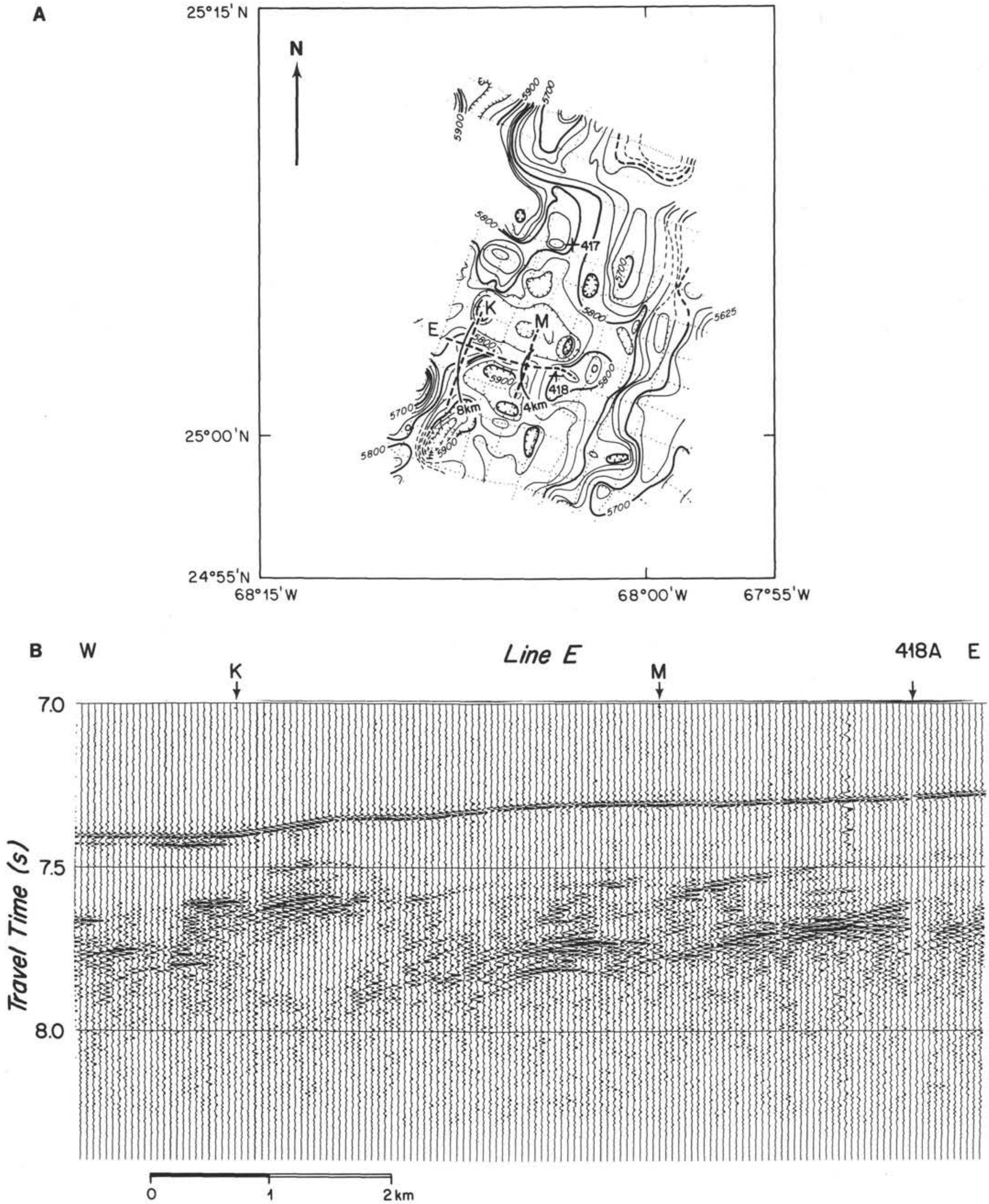

Figure 25. Water gun reflection profiles (from Auroux and Stephen, 1986). A. Location of profiles (dotted lines) on depth-to-basement map from Senske and Stephen (this volume). Solid arcs show entry points of rays displaying traveltime anomalies in 4- and 8-km circles discussed in text. Crosses show locations of Sites 417 and 418. B. East-west profile (E) crossing within 0.15 km of Hole 418A. C. Southwest-northeast profile (M) across 290° traveltime anomaly observed in 4-km circles. D. Southwest-northeast profile (K) across 290° anomaly observed in 8-km circles.

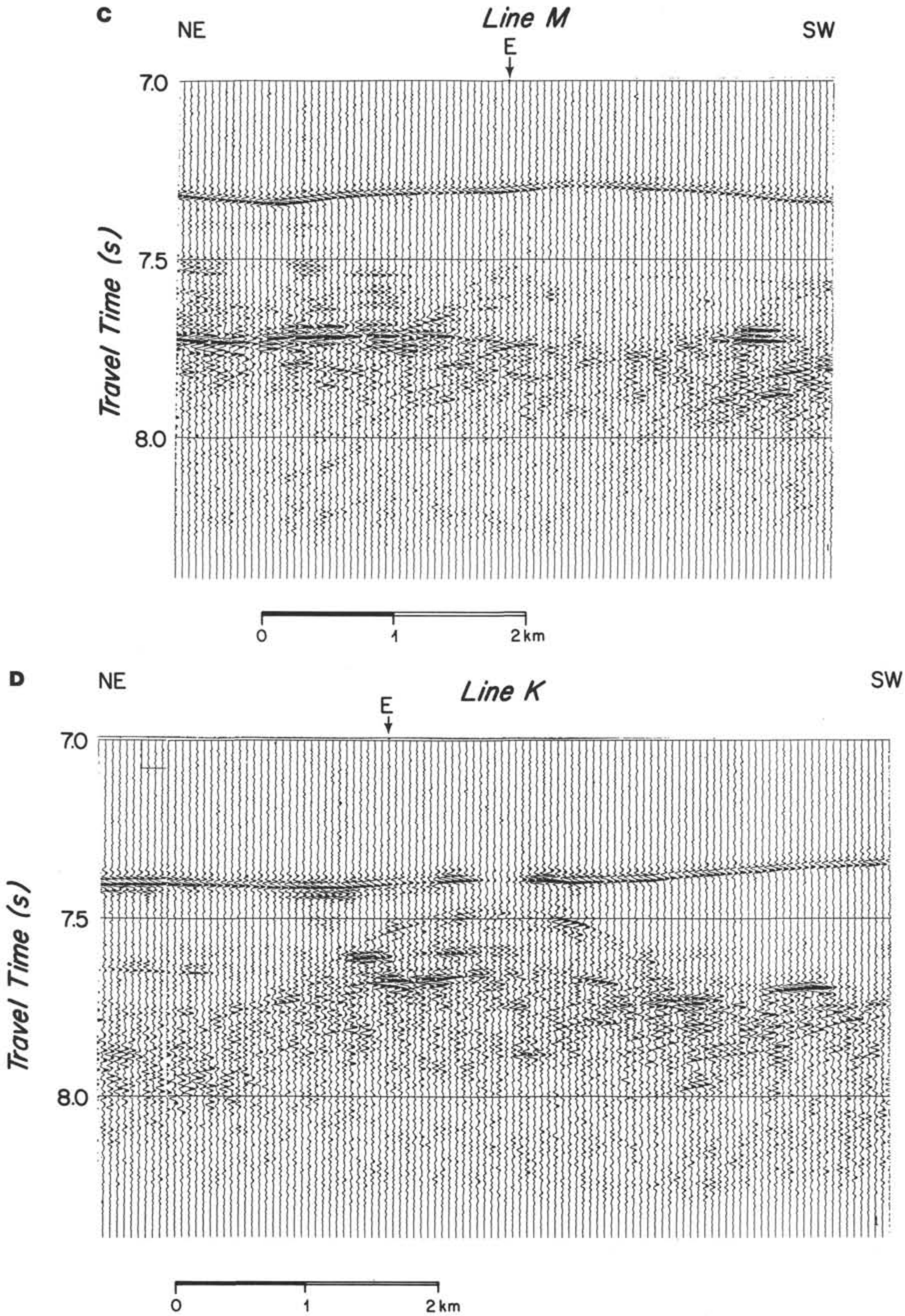

Figure 25. (continued).